UNIVERSITY OF CALIFORNIA SAN DIEGO

Comprehensive Study from Neutron Detection to Neutron Capture Therapy: Exploring Hydroxyapatite-Based Materials for Innovative Cancer Treatment Solution

A Thesis submitted in partial satisfaction of the requirements
for the degree Master of Science

in

Materials Science and Engineering

by

Yiwen Ji

Committee in charge:

Professor Olivia A. Graeve, Chair
Professor Shengqiang Cai
Professor Andrea Tao

2025

The Thesis of Yiwen Ji is approved, and is acceptable in quality and form for publication on microfilm and electronically.

University of California San Diego

2025

DEDICATION

I would like to express my sincere gratitude to my parents, Haodong Ji and Yanfeng Hou, for financially and spiritually supporting my Master's studies in the U.S., allowing me to pursue my dream in science.

I am deeply thankful to my advisor, Dr. Olivia Graeve, for granting me the freedom to choose the research topic that interests me the most. I also extend special thanks to Katya, Fabian, and the entire research group for their continuous and thoughtful guidance, which ultimately shaped this thesis into an acceptable form.

Moreover, I want to express my appreciation to all my friends, Xuan "Monica" Wang and Jiayu "Zoey" He, for always sharing happy and supportive conversations with me, no matter the distance. Also, I am grateful for the beautiful voices of Cyndi Wang and Silence Wang, which have kept me energized and uplifted throughout this journey.

Last but not least, I want to thank the 23-year-old and 24-year-old me for never giving up and for persevering through the challenges of completing such a lengthy thesis, driven by a long-term passion for science.

TABLE OF CONTENTS

LIST OF FIGURES

LIST OF TABLES

LIST OF ABBREVIATIONS

NCT: Neutron Capture Therapy

BNCT: Boron Neutron Capture Therapy

HAp: Hydroxyapatite

BHA: Boron-doped Hydroxyapatite

LET: Linear Energy Transfer

eV: Electron Volts

NAA: Neutron Activation Analysis

Z: Higher Atomic Numbers

GM: Geiger Müller

PMT: Photomultiplier Tube

PSD: Pulse-Shape Discrimination

AIE: Aggregation-induced Emission

LAB: Linear Alkylbenzene

PXE: Phenyl-o-xylylethane

PVT: Polyvinyltoluene

PS: Polystyrene

TADF: Thermally Activated Delayed Fluorescence

LiI: Lithium Iodide

LiF: Lithium Fluoride

BGO: Bismuth Germanite

PET: Positron Emission Tomography

ECE: Electron Collection Efficiency

Gy: Gray

Sv: Sievert

ESD: Electron Spin Resonance Dosimetry

TLD: Thermoluminescent Dosimeters

OSLD: Optical Stimulated Luminescent Dosimeters

BSH: Sodium Borocaptate

BPA: Boronophenylalanine

BET: Brunanuer-Emmett-Teller

FTIR: Fourier-Transform Infrared Spectroscopy

CaP: Calcium Phosphate

RBE: Relative Biological Effects

CBE: Compound Biological Effects

MSGCs: Microstrip Gas Chambers

GEMs: Gas Electron Multipliers

MICRO-Mesh Gaseous Structures: Micromegas

RPCs: Resistive Plate Chambers

ML: Machine Learning

AI: Artificial Intelligence

ACKNOWLEDGEMENTS

I would like to acknowledge that grammar revisions are done with the help of the writing center at UC San Diego and ChatGPT.

VITA

2023 Bachelor of Engineering in Materials Science and Engineering, Shenzhen MSU-BIT University;
Bachelor's degree in Chemistry, Physics, Mechanics of Materials, Lomonosov Moscow State University

2025 Master of Science in Materials Science and Engineering, University of California San Diego

ABSTRACT OF THE THESIS

Comprehensive Study from Neutron Detection to Neutron Capture Therapy: Exploring Hydroxyapatite-Based Materials for Innovative Cancer Treatment Solution

by

Yiwen Ji

Master of Science in Materials Science and Engineering

University of California San Diego, 2025

Professor Olivia A. Graeve, Chair

Cancer has been lethal and with absent effective remedies that many people can afford. Researchers have explored various therapeutic approaches for cancer treatments so far. However, most of the current therapies, such as surgery and chemotherapy [1, 2], suffer from prominent shortcomings, such as systemic toxicity and undesirable side effects. As a result, innovation in effective and affordable cancer treatments remains a critical challenge. Neutron detection is a

seemingly unrelated established field to biomedical applications, while it leverages its potential in cancer treatment.

This thesis aims to connect the established fields in neutron detection, dosimetry, and neutron capture therapy with material innovations to advance cancer treatment. The proposed therapeutic design involves delivering boron atoms through a nanovehicle and triggering the boron-neutron interaction specifically in tumor cells. To enable effective boron neutron capture therapy (BNCT), additional factors must also be considered. First, neutrons with varying energies and fluence can treat different kinds of cancer. For instance, fast neutrons are mainly used to treat tumors deep inside the body, while (epi)thermal neutrons are used for surface-level tumors. Therefore, neutron detectors are included in BNCT applications to study neutron characteristics (*e.g.*, energy and fluence) [3, 4]. In addition, dosimetry is important in BNCT applications to absorb and measure therapeutic radiation doses. Because tumor cells are localized compared to the applied radiation, luminescent dosimetry is expected to quantify the total radiation doses by analyzing luminescence spectra and absorb excess radiation that might affect surrounding healthy tissues.

Throughout an extensive literature review, this thesis identifies that hydroxyapatite (HAp) is a promising material that can absorb and measure radiation doses. This capacity mitigates the harmful effects of radiation on healthy cells and helps researchers quantify radiation exposure. Moreover, the well-established biocompatibility of HAp makes it suitable for tissue regeneration following tumor removal. This thesis also proposes that boron-doped hydroxyapatite (BHA) enhances the effectiveness of BNCT due to boron's tumor selectivity, enhanced bioactivity, biocompatibility, and biodistribution.

Overall, this thesis explores the relationship between neutron detection and cancer treatment. It provides a comprehensive review of conventional materials across these disciplines and highlights the potential of HAp and BHA in luminescence dosimetry and BNCT. By integrating three traditionally separate fields in neutron detection, dosimetry, and BNCT, this study offers novel insights into developing safer, more precise, and more efficient cancer treatment.

Introduction

Cancer remains one of the leading causes of death worldwide. To understand the complexity of tumor pathophysiology and improve treatment outcomes [5], researchers have developed numerous therapeutic strategies over the past decades. Among these, surgery, chemotherapy, and radiotherapy are the most established treatment modalities [1, 2]. However, these traditional approaches face significant limitations, including high costs, systemic toxicity, suboptimal efficacy, and collateral damage to surrounding healthy tissues [2, 6]. As a result, there is an urgent need for more precise, effective, and accessible cancer treatments.

Although neutrons are abundant in nature, they cannot be directly detected by human senses and are challenging to study experimentally. In 1930, Bothe and Becker observed a highly penetrating radiation emitted from certain elements, such as beryllium, under alpha particle bombardment. However, they misidentified this radiation as γ-rays [7]. It was not until 1932 that James Chadwick correctly identified this phenomenon as a new, electrically neutral subatomic particle, the "neutron" [6]. Subsequent research revealed that neutrons are composed of quarks bound by the strong nuclear force and possess a magnetic spin of 1/2 [8, 9]. Neutrons are unstable outside the atomic nucleus, complicating their detection and experimental study [2, 10]. This challenge has driven nearly a century of innovation in neutron detection technologies.

As these techniques advanced, it was discovered that neutrons interact with matter to produce secondary ionizing radiation (*e.g.*, gamma radiation and α/β particles), which have diverse biological effects [11]. Owing to their high penetration depth in biological tissues, neutrons have found valuable applications in radiation biology and nuclear medicine [12]. A particularly promising application is targeted neutron delivery, which aims to concentrate therapeutic neutron doses at tumor sites while minimizing damage to healthy tissue [5, 6, 13, 14]. To address this challenge, neutron capture therapy (NCT) was first proposed by Locher in 1936 [15]. Among

various neutron capture agents, boron stands out due to its large neutron capture cross-section at thermal and epithermal energies and the high linear energy transfer (LET) of its interaction products.

Nevertheless, neutron exposure also presents serious health risks, including non-stochastic and deterministic effects such as immune suppression, birth defects, and increased cancer risk [16]. According to the 2000 UNSCEAR report, the average person is exposed to only 0.1 mSv of neutron radiation per year [12]. This indicates a negligible public risk in everyday life. However, certain populations, such as astronauts, workers in neutron-emitting environments (*e.g.*, borehole exploration), and residents at high altitudes, may receive disproportionately higher exposures [17]. Because ionizing radiation is invisible and cannot be directly sensed, the development of reliable materials and technologies capable of accurately detecting, quantifying, and monitoring neutron radiation is essential. These technologies not only enhance safety in radiation environments but are also critical to the effectiveness of neutron-based therapies [12].

Among various biomaterials studied for radiation-related applications, hydroxyapatite (HAp), especially in nanoparticle form, has attracted significant attention. Figure 1 illustrates HAp's crystalline structure. As the primary mineral component of bone, HAp possesses several properties critical to biomedical applications, including biocompatibility, non-toxicity, pH-responsiveness, controlled ion release, and biodegradability. These characteristics make HAp a strong candidate for tissue engineering and drug delivery systems [18, 19, 20]. Moreover, HAp's tissue equivalence, thermoluminescent behavior, high sensitivity to ionizing radiation, and mechanical rigidity suggest its suitability for use in thermoluminescent dosimetry systems, especially under high-dose or long-term exposure scenarios [19, 21, 22].

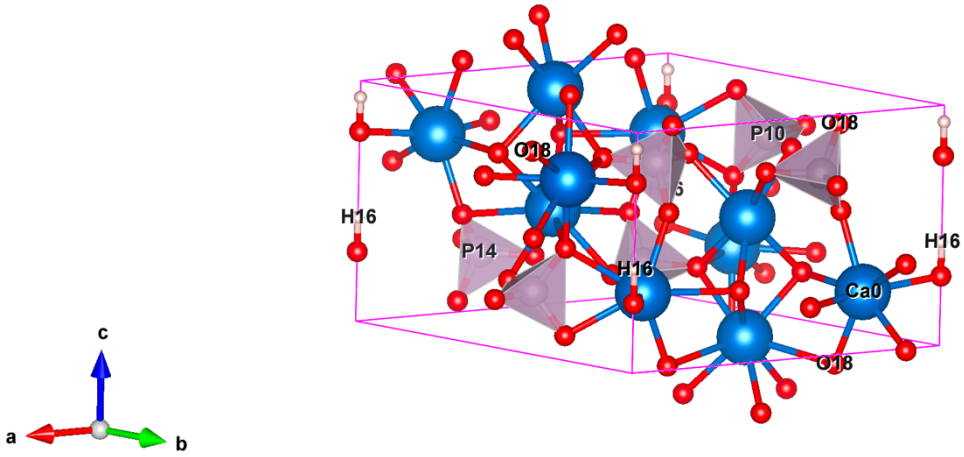

Figure 1. The crystal structure of hydroxyapatite, chemically defined by $Ca_{10}(PO4)_6(OH)_2$. The figure is generated in VESTA.

Boron is naturally found in bone and serves as an essential trace element in human physiology, particularly for bone health. Compounds such as boric acid (H_3BO_3) have been shown to elevate osteocalcin levels in postmenopausal women [23], promote osteoblast proliferation and differentiation, and influence hormone and micronutrient absorption [24]. In addition to these physiological roles, boron exhibits cytotoxic effects at elevated therapeutic concentrations, which can be harnessed to selectively damage tumor cells upon neutron capture [25, 26]. Furthermore, tumor cells can absorb boron atoms well, improving selectivity for targeted cancer treatment [27]. Leveraging these advantages, researchers have explored doping strategies to further tailor HAp for advanced biomedical applications. Of particular interest is boron-doped hydroxyapatite (BHA), chemically represented as $Ca_{10}[(PO_4)_{6-x}(BO_3)_x][(BO_3)_y(BO_2)_z(OH)_{2-3y-z}]$ [28]. By substituting boron-containing ions such as BO_3^{3-} or BO_2^- into the HAp lattice, BHA integrates the biological and structural advantages of HAp with the neutron capture potential of boron. These modifications have been shown to enhance protein adsorption, ion release, and cell viability, without compromising HAp's mechanical integrity [23, 24, 29].

Furthermore, BHA exhibits pH-sensitive degradation, a particularly advantageous property for targeted neutron delivery. This property enables BHA to degrade and release boron specifically in the acidic microenvironment of tumor tissues [30], thereby improving therapeutic selectivity and minimizing toxicity to healthy tissues [31].

Despite this promise, HAp remains underexplored in radiation dosimetry, and BHA is still in the early stages of exploration for Boron Neutron Capture Therapy (BNCT), a cancer treatment modality that relies on neutron-induced nuclear reactions. This thesis aims to explore the structural feasibility, radiation interaction characteristics, and biomedical potential of HAp and BHA in the context of neutron-mediated cancer therapies. Chapter 1 introduces the fundamental physics of neutron interactions and provides a comprehensive overview of neutron detection principles. Chapter 2 reviews materials commonly used in neutron detectors. Then, Chapter 3 focuses on radiation dosimetry, emphasizing the measurement and evaluation of the biological effects of neutron detection. Lastly, Chapter 4 investigates BNCT, a cutting-edge cancer treatment that utilizes neutron-material interactions at the cellular level. Throughout these chapters, special emphasis is placed on the design, characterization, and application of hydroxyapatite and boron-doped hydroxyapatite for both neutron detection and therapy. The thesis concludes by outlining key research directions to accelerate the integration of materials science into neutron-based biomedical technologies.

Chapter I. Background Information on Neutrons and Neutron Detection

1.1. Neutron Sources

Neutrons cannot be produced through traditional radioactive decay processes, such as the emission of gamma rays via beta decay [32]. Instead, only specific methods can set neutrons apart from nuclei, including neutron generators, (α, n) reactions, fusion reactors, nuclear fission, and spallation. Neutron generators produce a single neutron with an energy of several MeV by colliding specific target nuclei, usually D-D ($^{2}H+^{2}H \rightarrow {}^{3}He+n$) or D-T reactions ($^{2}H+^{3}H \rightarrow {}^{4}He+n$), as shown in Figure 2 [2, 12, 33].

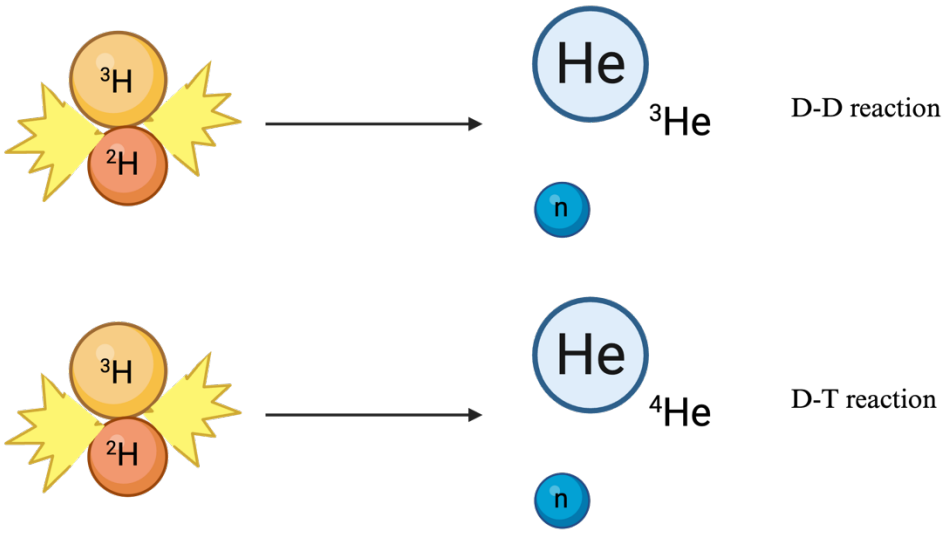

Figure 2. D-D and D-T reactions in neutron generators.

Processes such as (α, n) reactions, fusion, fission, and spallation, are required for generating many neutrons [2]. In (α, n) reactions, alpha particles emitted from radioactive isotopes (*e.g.*, ^{226}Ra, ^{227}Ac, ^{239}Pu, ^{238}Pu, ^{241}Am, and ^{244}Cm) interact with light-weighted nuclei (*e.g.*, Be) to produce neutrons, as shown in Figure 3 [12, 32]. For example, one of the alpha-neutron reactions produces neutrons via the reaction $^{4}_{2}\alpha + {}^{9}_{4}Be \rightarrow {}^{12}_{6}C + {}^{1}_{0}n$ (see Figure 3) [2]. Because the energy of the

neutrons depends on the energy of the alpha particles and the target nucleus, the resulting neutron energy spectrum closely follows the alpha energy distribution, enabling accurate predictions of the neutron yield and energy spectrum [32]. Neutrons generated by (α, n) reactions offer better flux uniformity within the target volume, although they exhibit lower cross-sections and are generally used for limited analyses [34].

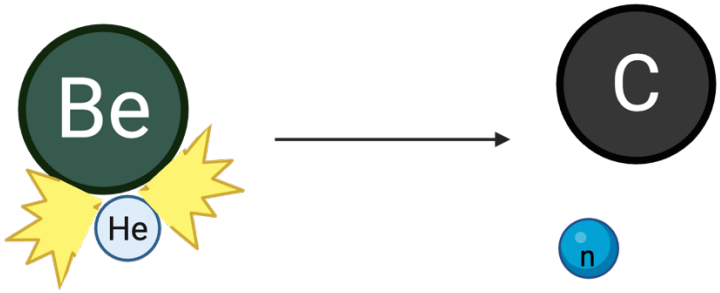

Figure 3. The alpha-neutron reaction.

Fusion reactors also produce neutrons, typically energetic ones with an average energy of 14 MeV, as byproducts of the D-T reaction [2]. Fusion reactors can generate the required power and activate reactor materials to produce radioisotopes. However, the high-energy neutrons they emit pose significant challenges for radiation shielding and protection [2]. In addition, nuclear fission refers to the spontaneous process in which heavy fissionable nuclei capture a slow neutron and split it into two fission fragments, releasing a large amount of high-energy (fast) neutrons and triggering further fission events [10, 12, 35]. Figure 4 illustrates the nuclear fission process. Typical fissionable nuclei include ^{252}Cf, ^{235}U, ^{239}Pu, and ^{233}U, which are transuranic elements with atomic numbers higher than uranium [32, 36, 37]. In fission devices, thick containers are usually used to exclusively emit neutrons and gamma radiation as well as to encase fissionable materials that raise safety concerns due to their radioactive nature [32]. However, nuclear fission presents

disadvantages, such as high replacement costs and the need for frequent neutron flux calibration due to their short half-lives and poor flux uniformity [34].

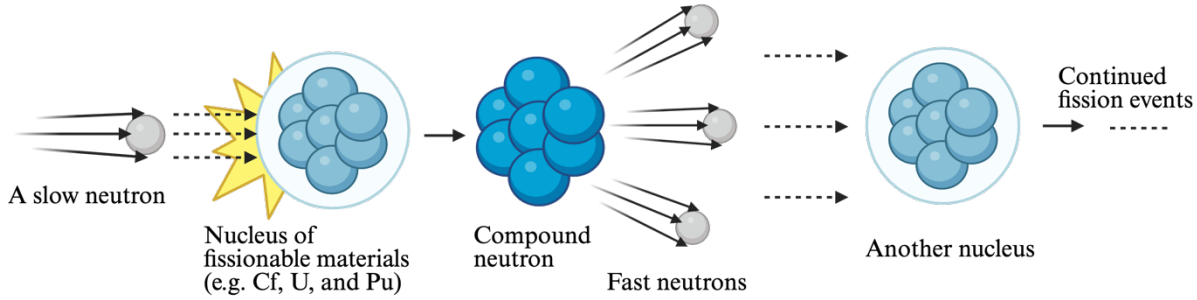

Figure 4. Schematic illustration of the nuclear fission process.

Lastly, spallation refers to the process where high-energy neutrons bombard and transfer their energy to heavy nuclei, producing protons, gamma radiation, and neutrons with energies in the MeV range, as shown in Figure 5 [10, 38]. The heavy nuclei are usually tungsten or lead, undergoing the spallation process in extreme environments, such as through cosmic ray interactions [2, 8]. Spallation holds promise for large-scale applications such as the disposal of nuclear waste in underground repositories [37]. The main difference between nuclear fission and spallation is that fast neutrons are involved in any phase of the spallation, whereas they are only involved in the generation phase of the fission process.

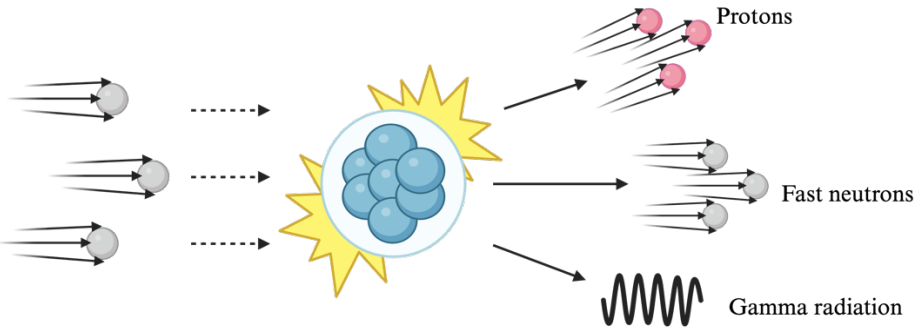

Figure 5. Schematic illustration of the spallation process

1.2. Neutron Energy

Neutron energies vary depending on their sources, and these variations are critical for different applications due to their unique characteristics (see Table 1). In neutron detection, energy is typically measured in electron volts (eV), with ionizing radiation commonly reported in units of keV or MeV. Although the lower and upper bounds of neutron energy are clearly defined, specific values may differ slightly between studies. The lower energy limit refers to the threshold required for ionizing materials to generate secondary charged particles, while the upper limit is defined by nuclear science considerations. Neutron energies are generally classified, ranging from low to high, as cold, thermal, epithermal, and fast neutrons, as shown in Table 1. Cold neutrons have energies in the meV or sub-meV range, typically observed at temperatures approaching absolute zero. Thermal neutrons have an average energy of approximately 0.025 eV. Epithermal neutrons fall within the eV to several hundred keV range, and neutrons with higher energies are classified as fast neutrons [39].

Table 1. Types of neutrons with different energies and their applications.

Classifications	Energy	Characteristics [39].	Applications
Cold Neutrons	10^{-4}-0.01 eV, at temperatures approaching 0 K.	Low energy	a. Investigation of magnetic materials and biological samples [39]. b. Neutron scattering experiments to study crystal structures and phase transitions under low thermal excitations [39]. c. High-resolution measurements in condensed matter research, offering improved precision in structural characterization [40].
Thermal Neutrons	0.01-0.1 eV, with an average of 0.025 eV, depending on moderator types or temperatures.	In thermal equilibrium with a medium at the room temperature.	a. Enhancement of neutron capture reactions and improved stability and efficacy of nuclear processes [39]. b. Non-destructive analysis of internal defects and material structures to support geophysical studies, such as understanding volcanic eruptions and earthquakes [41]. c. Use of accelerator-based thermal neutrons in biomedical applications, including treatment of skin melanoma via BNCT [3].
Epithermal Neutrons	0.1-5×10^5 eV		a. Deeper tissue penetration using epithermal and fast neutrons, enabling treatment of deeper lesions in biomedical research [5]. b. Application of neutron activation analysis (NAA) to quantify the types and concentrations of specific elements in biological, geological, and industrial samples [42].

Fast Neutrons	Higher than 5×10^5 eV	Some materials have comparable fast neutron cross-sections, their effectiveness in fast neutron detection is not strongly affected by material type.	a. Cancer therapy [4]. b. Non-intrusive neutron-based scanning for detecting prohibited items including explosives, smuggled goods, and narcotics [43]. c. Determination of surface composition in geological research through fast neutron leakage flux measurements [44].

1.3. The Applications and Impacts of Neutrons

Neutrons play an important role in many scientific fields. Key neutron applications include nuclear physics (such as fusion and fission), materials characterization through scattering and diffractometry, and radiation dosimetry for personal protection [45]. In materials science research, neutrons can deeply penetrate materials to centimeters without altering the radiation's inherent properties, as the inability to interact with electrons [12]. For example, researchers can use neutrons to study the internal structure of materials that are often inaccessible to X-rays [8]. In radiation biology, nuclear medicine, and cancer therapy, researchers can study molecules by shooting neutrons at biological samples [46, 47].

1.4. Introduction to Neutron Detection

1.4.1. Principle of Neutron Detection

Neutron detection relies on indirect methods, using neutron–nucleus interactions to produce charged particles that generate measurable electric signals [48]. Neutrons, however, do not directly produce electrons or radiation, making them undetectable by conventional means. To

detect neutrons using traditional detection systems, neutrons need to be converted into charged particles, such as alpha or beta particles, or gamma radiation. This conversion is based on the interaction of neutrons with atomic nuclei via nuclear reactions or recoil mechanisms, depending on the neutron energy [48]. Once converted, these particles transfer the kinetic energy of neutrons to the surrounding material, causing ionization. For example, alpha particles transfer energy through interactions with electrons that create excited atoms or ion pairs. Gamma rays, on the other hand, transfer energy through Compton scattering, photoelectric absorption, or pair production [32]. The resulting ionization generates electrical signals that can be captured by traditional detection or signal processing systems [8]. Researchers can then analyze these signals to obtain information about neutrons.

1.4.2. Mechanisms of Neutron Detection

Depending on the initial energies and materials, neutrons have various mechanisms of interaction with nuclei [36]. Neutron-nucleus interactions involve two mechanisms, the recoil mechanism and the reaction mechanism, illustrated in Figure 6 and Table 2. The recoil mechanism, also referred to as (n, n'), where n' denotes the recoiling nucleus, involves a physical reaction in which kinetic energy is transferred from neutrons to target nuclei upon collision. The recoiling nuclei gain energy and become charged, enabling them to further ionize the surrounding detector medium. In elastic scattering, neutrons may transfer nearly all of their energy, whereas in inelastic scattering, only a portion of their corresponding energy is transferred. The amount of energy imparted depends on the angle and mass of the recoiling nucleus. The recoil energy is proportional to the energy of the incident neutron. When the recoil occurs at 0°, the energy transfer is maximized. This method is particularly useful for measuring the energy spectrum of fast neutrons. According to the principles of energy and momentum conservation, this technique is best suited for fast

neutrons interacting with light nuclei such as hydrogen or helium, as these allow for maximal energy transfer and efficient charge generation [32, 39].

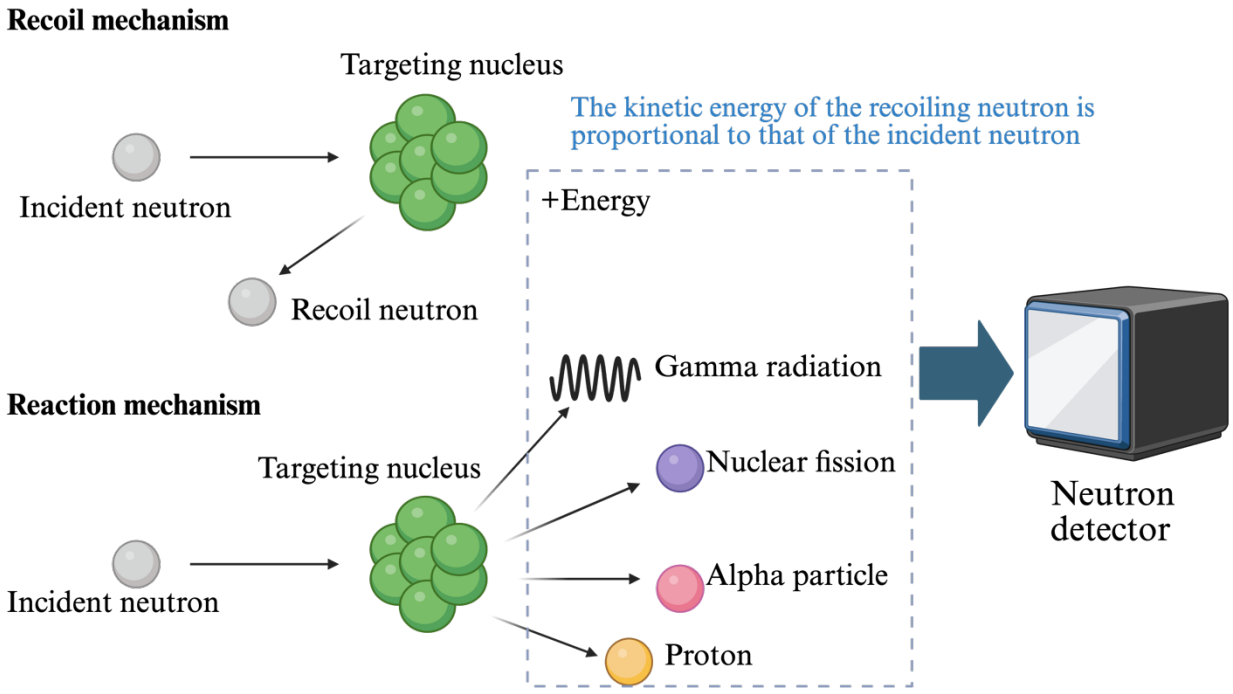

Figure 6. Visualization of two neutron interaction mechanisms, namely recoil and reaction. The recoiling angle for each reaction product is only for illustration purposes and has no relationship with the real case. The figure is created by the author, based on the description from [32, 39].

Table 2. Neutron-nuclear interaction mechanisms.

Interacting types	Mechanisms [32]	Examples [36, 39]
Recoil	Neutrons are scattered by a nucleus, transferring all or part of their kinetic energy. If the recoiling nucleus receives sufficient energy, it can ionize the surrounding material at the point of interaction.	• Elastic scattering • Inelastic scattering
Reaction	A neutron may induce a nuclear reaction, and the resulting reaction products, such as protons, gamma rays, alpha particles, or fission fragments, initiate the detection process.	• Radiative Capture • Nuclear fission • Spallation • Nuclear reactions, such as $^{10}B(n, \alpha)$, $^{6}Li(n, \alpha)$, and $^{3}He(n, p)$

Another neutron interaction mechanism is through nuclear reactions, which involve radiative capture (n, γ), nuclear fission (n, fission), and particle emission reactions such as (n, p) or (n, α) [32]. Radiative capture occurs when a neutron is absorbed by a nucleus, forming an excited and often radioactive compound nucleus that subsequently emits one or more gamma photons to return to a stable ground state [49]. This process, known as neutron activation, is a primary method in activation analysis for measuring neutron intensity. It is commonly used to study materials such as ceramics and determine trace element concentrations by analyzing the emitted gamma radiation [50]. Both inelastic scattering and radiative capture can result in gamma emission from an excited compound nucleus. However, only radiative capture always produces a radioactive compound that undergoes decay, while inelastic scattering does not. Nuclear reaction interactions can also take place through nuclear fission and spallation, both of which were previously discussed in the neutron source section (see Figures 4 and 5).

1.4.3. Important Parameters of Neutron Detection

Cross-sections, usually noted as σ, represent the effective area of a target nucleus available to absorb neutrons. Due to the variety of neutron–nucleus interaction mechanisms, researchers have defined different types of cross-sections for each interaction. For instance, neutron capture and neutron absorption cross-sections are used to quantify the probability of a neutron reacting with a nucleus [2, 8]. These variations are summarized in Figure 7 and Table 3. The greater the cross-section of a material, the more likely it is to absorb neutrons, resulting in higher detection efficiency [8]. Therefore, detector materials with large cross-sections are preferred. For example, the neutron absorption cross-section of a widely used ^{3}He material exceeds 10^{4} barns, which is a thousand orders of magnitude larger than that of most materials [8]. Thus, materials selection with sufficiently high cross-sections is a prerequisite for effective neutron detection.

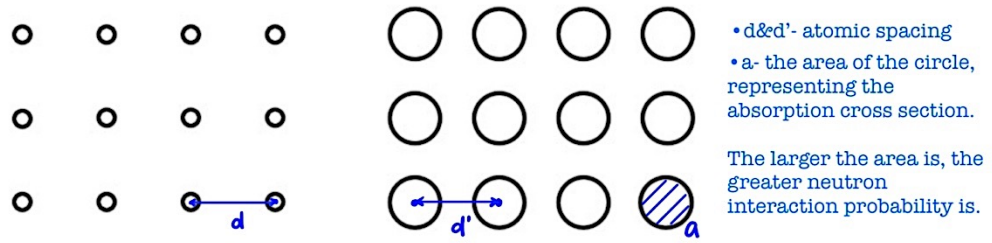

a) b)

Figure 7. Conceptual comparison of cross sections for arbitrary materials. Materials that have a) smaller and b) larger cross sections. The figure is adapted from [8].

Table 3. Descriptions of scattering and neutron capture cross-sections.

Scattering Cross-Sections [51]	In the context of elastic and inelastic scattering, neutron interactions with matter are quantified by a parameter known as the cross section. This parameter represents an effective area that correlates with the probability of a specific radiation–target interaction. The larger the cross section, the more likely a neutron is to interact with a given target nucleus.
Neutron Capture Cross-Sections (or Neutron Absorption Cross Sections) [39]	The term "neutron capture cross sections", typically represented by σ, refers to the probability that an incident neutron will be absorbed by a nucleus, leading to a nuclear reaction. The neutron capture cross section effectively describes the area that a nucleus presents to an incoming neutron for the absorption process to occur. The standard unit for cross section is the barn, where 1 barn = 10^{-24} cm^2.

1.4.4. Operation Modes of Neutron Detectors

Neutron detectors are traditional detection systems that interact with neutrons and produce charged particles or radiation. Common classifications of neutron detectors include gas-filled, scintillator, and semiconductor detectors, depending on their detection mechanisms and materials [39]. Neutron detectors work in three distinct modes to process particles or radiation, and produce different signals based on various interaction mechanisms. The working modes of neutron detectors include the pulse mode, the current mode, and the mean square voltage mode [32].

The detector that works in the pulse mode records a single neutron interaction event and produces a series of voltage pulse signals that are directly correlated to the charge [52]. Therefore, detectors working in the pulse mode are useful in spectroscopy, where they are required to record a single neutron interaction event [32]. The pulse strength and shape of the detector can discriminate against the gamma radiation contribution. However, at high neutron flux, pulse mode becomes less effective for gamma discrimination and may yield inaccurate results [52].

The issue of inducing inaccurate results in high flux environments in the pulse mode can be addressed by using the current mode. For example, in the current mode, neutron detectors record multiple events and generate the average current, representing the time-averaged signal [52]. The detectors in the current mode are useful in measuring neutron noise and extracting kinetic reactor parameters [53]. Owing to the production of the average current, the current mode detectors are impractical for gamma radiation discrimination [52]. As neutron flux increases further, the mean square voltage output of neutron detectors records fluctuations in mixed radiation fields and produces signals that are proportional to both the square of the charge and the event rate [54]. The illustrated explanations of the difference among these three modes can be found in Figure 8 with the help of the pulse height spectrum, one of the outputs of neutron detection.

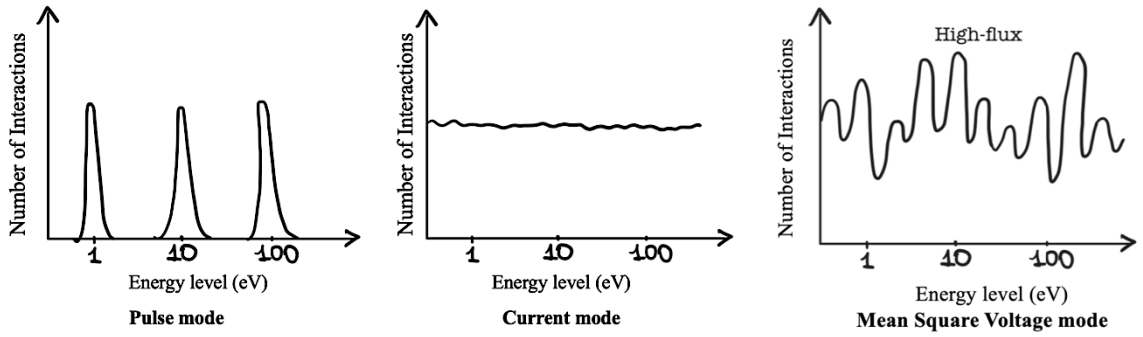

(a) (b) (c)

Figure 8. The three operation modes of neutron detectors: pulse mode (a), current mode (b), and mean square voltage mode (c). It should be noted that the x-axis values are schematic and not intended to represent the true measurement scale used in practical detector systems. The figure is created by the author, based on the description from [54].

1.4.5. Detection Outputs of Neutron Detectors

Current detection technologies for extracting neutron information allow for measurement of neutron flux, energy spectra, and neutron counts. One common technique that was mentioned in section 1.4.4 is the pulse height spectrum. As shown in Figure 8, the pulse amplitude distribution

reveals information about neutron energy and flux. Then, the obtained energy and flux information is able to determine the type of radiation involved, the charge generated, and the performance of the detector [32]. Another method to obtain neutron energy information is through neutron energy spectra via techniques such as radiation spectroscopy, time-of-flight measurements, and helium spectrometers [48]. One key metric in energy spectra is energy resolution, which determines how accurately the detector distinguishes between different energies. For instance, in differential spectra, a pulse with a larger width may represent greater signal fluctuation, even if it deposits the same energy as narrower pulses. However, retrieving energy information is often challenging and may not be necessary for all applications, as it can sometimes be inferred from detector type and surrounding materials [48].

In addition, detection efficiency ensures that the generated pulse is large enough to be recorded as detector's output. Two types of efficiencies are involved, absolute and intrinsic detection efficiencies, representing the ratio of pulse counts to the total number of radiation quanta emitted by the source and to the number of quanta reaching the detector, respectively. The efficiency of detecting neutrons is usually below 100% because this uncharged radiation will travel long distances [8].

1.4.6. Applications of Neutron Detection

In addition to their broad applications, neutrons are valuable in scientific research through their detection capabilities (see Table 4). The most fundamental and widely recognized use of neutron detection is physics research in nuclear reactions. With growing concerns over harmful radiation and the pursuit of effective cancer treatments, researchers have increasingly explored neutron detection in dosimetry and radiotherapy. One such method, neutron capture therapy, has been under clinical investigation since the 1950s [5]. However, the full potential and

implementation of neutron dosimetry and radiotherapy applications are still not widely understood or adopted.

Table 4. Applications of neutron detection.

Application Classifications	Examples
Nuclear Physics	Fusion and fission [45]
Specific Nuclear Materials	For applications that require instruments that can sensitively detect or characterize uranium or plutonium isotopes under challenging conditions, such as arms control, material safeguards, or facility decontamination and decommissioning [45]
Fundamental Science	Study of nuclear reaction cross-sections, dark matter, space physics, or neutron beams [45]
Dosimetry	For personnel protection or radiotherapy treatment [45]
Materials Science Research	a. Neutron scattering: Acquire the material information by complementing X-ray or gamma-ray radiation methods in neutron scattering, diffractometry, and tomography experiments [8]. b. Study the structure or dynamics of materials, especially magnetic materials [9]. c. Nuclear reaction monitoring, industrial non-destructive testing, and nuclear medicine imaging [39].
Other	Nuclear power plants, radioactive waste repositories, and nuclear medicine [2, 55]

Chapter II. Neutron Detector Materials

2.1. Introduction to Neutron Detector Materials

To maximize the efficiency of neutron-to-signal conversion and provide structural integrity to the detector, the selection of suitable materials has long been a central focus in detector design. A wide range of materials, gaseous, solid, and liquid, have been employed in detectors [48]. These materials have distinct characteristics specific to applications. Therefore, material requirements vary depending on the intended use. The underlying requirement is detection efficiency. Denoted by the Greek letter ε, detector efficiency represents the ratio of the number of recorded neutrons incident on the detector per unit time. Detector efficiency has two correlated components of geometric and intrinsic efficiency. Specifically, geometric efficiency is determined by the physical configuration between the neutron source and the detector, while intrinsic efficiency is the fraction of neutrons absorbed by the detector material out of those that reach it [8]. The latter is strongly influenced by the material's neutron cross-section. To enhance overall efficiency, researchers may increase detector area (typically up to 1 m^2) or utilize hydrogen moderators to slow fast neutrons, thereby increasing the likelihood of interaction [2, 38, 39].

Another critical consideration in material selection is the signal-to-noise ratio, particularly the ability to distinguish between neutron signals and background gamma radiation. Gamma rays often induce unwanted ionization in the detector material, interfering with neutron detection [32, 39]. In scenarios where gamma radiation is considered background noise, effective gamma-neutron discrimination is essential. This is often quantified using the Q-value, which represents the energy released by the reaction products. A higher Q-value generally correlates with improved discrimination between neutron and gamma-induced events [2]. Additional factors also influence materials selection, including economic feasibility, compatibility with detector architecture,

resistance to thermal and mechanical stress, and the material's ability to undergo strong ionization following neutron–nucleus interactions [32, 38]. Given these general criteria, the following sections will examine material choices specific to different categories of neutron detectors, including gas-filled, scintillation-based, and semiconductor-based systems.

2.2. Discussion on Gas, Scintillator, and Semiconductor Detectors

2.2.1. Gas-filled Detectors

Gas-filled detectors have long been the most widely used type of neutron detectors due to their simplicity and effectiveness [56]. In general, as revealed in Figure 9, in a gas-filled detector, neutron interactions with gas molecules produce charged particles. These particles acquire kinetic energy and ionize the gas, generating positive and negative ion pairs under an applied voltage. After that, electrons drift toward the anode and positive ions toward the cathode, forming a measurable current [48].

The total number of ion pairs can be estimated by dividing the Q-value (the energy released during the interaction) by the W-value, which represents the average energy required to generate a single ion pair [8]. The number of ion pairs is directly proportional to the initial energy of charged particles and thus determines the magnitude of the resulting current. If the applied voltage, typically around 30 eV, is too low or improperly biased, electron recombination with positive ions may occur, resulting in no measurable signal output [48]. Several other factors influence signal generation, including the type of fill gas (*e.g.*, helium, boron trifluoride, hydrogen, or argon), the detector's geometric configuration, and the operational region determined by the applied voltage [57].

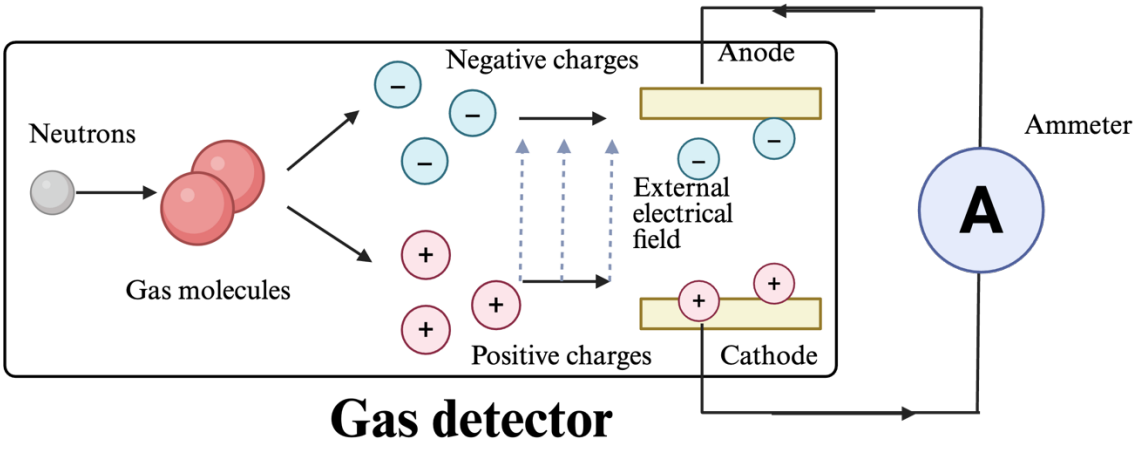

Figure 9. Schematic illustration of the gas detector mechanism. The figure is created by the author, based on the description from [48].

2.2.2. Materials Used in Gas Detectors

Among gas-filled materials, helium (^{3}He) is the most widely used due to its excellent properties for neutron detection. These include a high neutron absorption cross-section, low gamma-ray sensitivity, chemical inertness, and a favorable Q-value [2, 8, 58]. The primary neutron capture reaction in ^{3}He-based detectors is:

$$n + {}^3He \rightarrow {}^3H + {}^1H + 0.764\ MeV.$$

The energy released (0.764 MeV) is divided between the emitted tritium (^{3}H) and proton (^{1}H), which travel in opposite directions and ionize the fill gas to produce electron-ion pairs [59]. This energy is directly related to the detector's output pulse amplitude. Helium detectors typically operate at pressures between 10 and 20 atm, often mixed with quenching gases such as CO_2 or CF_4 to improve spatial resolution [59]. ^{3}He detectors are commonly used in neutron spectrometry, medical imaging applications such as MRI lung imaging [58], and general radiation monitoring [60]. Despite these advantages, ^{3}He is increasingly constrained by supply shortages and transportation challenges [58], motivating the search for alternative detector materials.

One such alternative is boron trifluoride (BF_3), enriched with the isotope ^{10}B. BF_3 is a cost-effective gas that compensates for helium shortages and is frequently used in proportional counters [48]. The relevant neutron capture reactions involve the following steps:

(1) $^{10}B+n \rightarrow {}^{7}Li^{*}+{}^{4}He+2.310$ MeV

(2) $^{7}Li^{*} \rightarrow {}^{7}Li+\gamma$ (0.48M eV)

The second reaction occurs in approximately 6% of cases, producing a secondary gamma photon [48]. BF_3 offers a higher Q-value than helium, enhancing gamma-ray discrimination [8], which is particularly beneficial in gamma-rich environments such as ultrashort-pulse laser neutron sources where BF_3 is often employed for neutron diagnostics [61]. BF_3 is also relatively easy to handle and economical, making it suitable for use in multi-detector arrays [60]. However, BF_3 has some disadvantages, such as its toxic and corrosive nature [62], limited temperature tolerance [2], and lower neutron detection efficiency, due to its relatively small neutron capture cross section [8].

As a further alternative, boron-lined detectors have been developed to address the shortcomings of both helium and BF_3 systems. These detectors utilize solid-state boron films (*e.g.*, B_4C) instead of gaseous targets, enabling the same nuclear reactions while offering improved detection efficiency, uniformity, and thermal stability [2, 48, 63]. Such systems are especially advantageous in applications requiring long-term stability or exposure to varying environmental conditions [64]. Other gases, such as hydrogen and methane, have been explored for fast neutron detection via elastic scattering processes [2], as well as in emerging gas detection sensors [65].

In addition to neutron-reactive gases, noble gases such as argon and xenon are frequently used as carrier or base gases in gas-filled detectors. Their interactions are based on radiative neutron capture reactions, such as Ar (n, ɣ) [66] and Xe (n, ɣ) [67]. These gases contribute to the detector's overall response and are often chosen for their high atomic number, inert nature, and

ability to support gas multiplication that occurs at higher applied voltage regions, such as in proportional and Geiger-Müller regions.

2.2.3. Voltage-Dependent Operational Regions in Gas-Filled Detectors

Gas detectors operate in three different applied voltage regions: (1) ionization chamber region, (2) proportional region, and (3) Geiger–Müller region, as shown in Figure 10. The materials mentioned above can operate in each region independently, depending on the applied voltages and geometry, each of which yields different output characteristics. The following section will describe the working principles, geometries, signal outputs, and fill gas choices associated with each region.

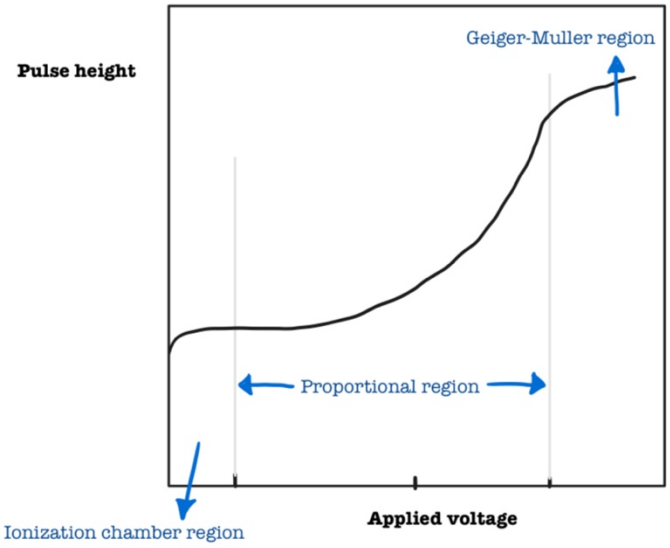

Figure 10. Three regions in gas-filled detectors: (1) Ionization chamber region, (2) proportional region, and (3) Geiger-Müller region. The figure is reproduced by the author, based on the description from [8, 48].

2.2.3.1 Ionization Chambers

a) Principles

Ionization chambers are regarded as the simplest type of gas-filled detectors. In this operational mode, a voltage is applied across a gas-filled enclosure, causing the formation of ion

pairs when ionizing radiation interacts with the gas. The resulting current is collected and measured using an ammeter connected to the external circuit. When the rate of radiation exposure is stable and ion recombination is negligible, the ionization current remains constant. The amount of charge collected at the electrodes is directly proportional to the energy deposited in the gas [32]. As the applied voltage increases, the drift velocity of the charged particles also rises. This reduces the likelihood of recombination, leading to a higher ionization current. Once all free electrons are efficiently collected and recombination is fully suppressed, the current reaches a plateau. In this saturation region, the current becomes dependent solely on the ionization charge density and drift velocity, assuming that all negative ions behave similarly to free electrons [56, 72]. Figure 11 illustrates the working principle in ionization chambers. Ionization chambers can operate in two modes, current and pulse mode. In the current mode, the detector measures a continuous ionization current. In pulse mode, it detects individual pulses generated by discrete radiation quanta, depending on the application [32].

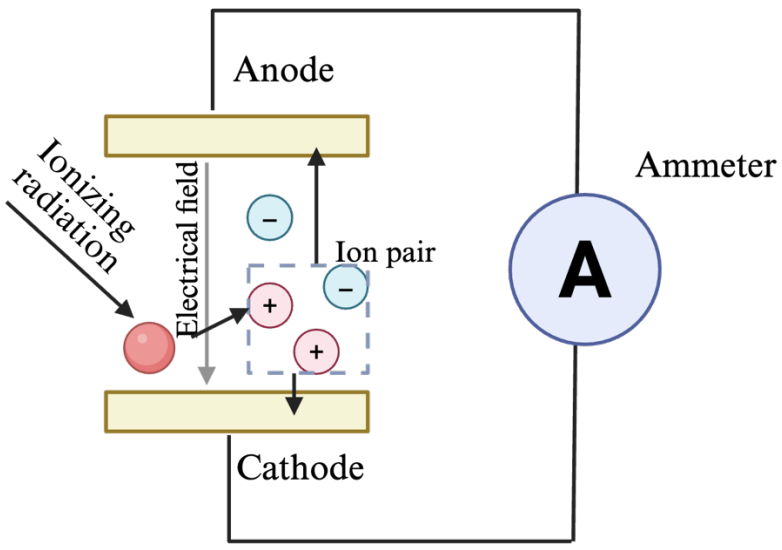

Figure 11. Schematic illustration of the working principle of an ionization chamber under applied voltage.

b) Fill gas

Gas-filled detectors can be constructed with a wide range of gases, depending on the detection objective. In principle, nearly any gas at pressures up to 1 atm can be used, including those with relatively high electron attachment coefficients. For general radiation detection, air is often employed due to its accessibility and simplicity, especially in measurements of gamma-ray exposure. However, for improved ionization performance and higher signal output, argon is commonly used because of its favorable ionization characteristics and higher electron yield per unit energy deposited [32].

2.2.3.2 Proportional counters

a) Principles

Proportional counters operate in the proportional region of gas-filled detectors, where the applied voltage is higher than that used in the ionization chamber region. As this voltage increases beyond a certain threshold, the resulting electric field becomes strong enough to accelerate free electrons to energies sufficient for secondary ionization through collisions with gas atoms [57]. This cascade of ionizations initiates a charge multiplication process, commonly known as an avalanche, as shown in Figure 12. The threshold electric field required for initiating this avalanche is approximately 10^6 V/m [32]. Importantly, the total number of charges produced during the avalanche remains proportional to the initial ionization caused by the incident radiation. This ensures a linear relationship between the energy deposited in the detector and the resulting pulse amplitude [8, 57]. The avalanche process terminates once all the electrons are collected at the anode [48].

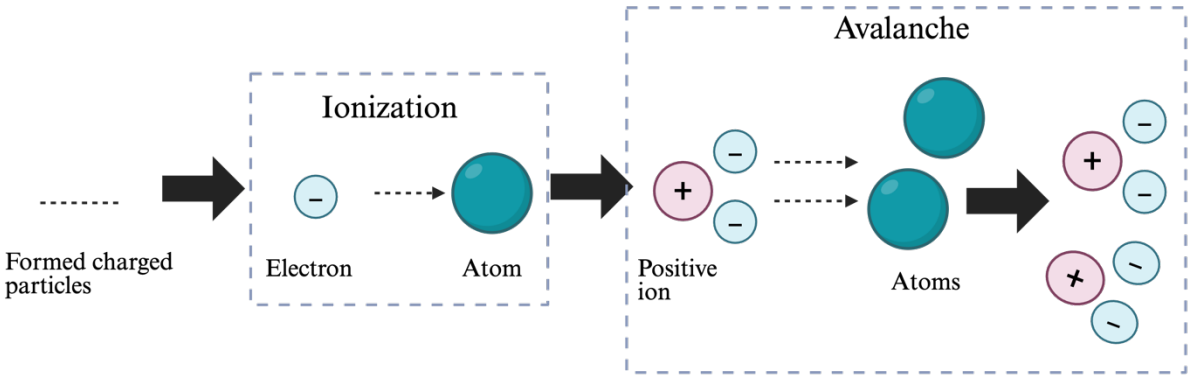

Figure 12. Schematic illustration of the avalanche process that occurs above the ionization chamber region. The figure is created by the author, based on the description from [8].

The built-in signal amplification provided by avalanche multiplication eliminates the need for an external amplifier, thereby improving the signal-to-noise ratio and enhancing the detector's sensitivity to low radiation levels [32]. These characteristics make proportional counters valuable in applications such as radiation dosimetry and reactor power monitoring. However, further increases in applied voltage can lead to the buildup of positive ions (space charge) near the anode. This space charge distorts the electric field and interferes with charge multiplication, thereby limiting the upper boundary of the proportional operating region [48].

b) Geometry of Proportional Counters

Proportional counters have two configurations, cylindrical and planar, as shown in Figure 13. The most common geometry of proportional counters is cylindrical, consisting of a thin anode wire positioned along the central axis of a hollow cylindrical cathode filled with gas. During operation, primary electrons drift toward the anode and undergo avalanche multiplication in the intense electric field near the wire. Because the avalanche occurs close to the anode and the resulting positive ions drift away slowly, the detector can register subsequent radiation events even

before all ions from the previous interaction have cleared. This behavior introduces a slight time delay between the initial ionization and the recorded output pulse [32, 57].

An alternative design for proportional counters is the planar configuration, in which the electric field is established between two parallel electrodes [8]. This configuration may be chosen for specific design or application requirements.

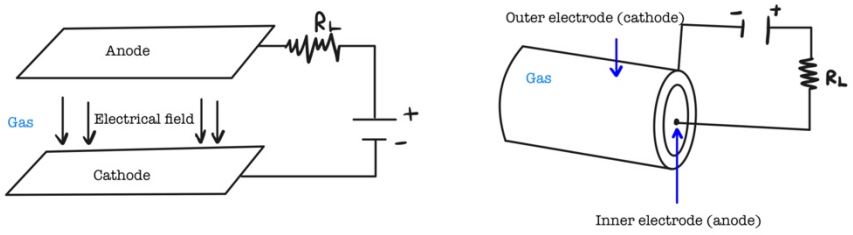

a) b)

Figure 13. a) The planar geometry; b) the cylindrical geometry of proportional counters. The figures are created by the author, based on the description from [8, 32].

Beyond basic geometry, proportional counters come in various structural designs, each optimized for specific detection environments and radiation types. A common design is the sealed tube detector, typically constructed with a stainless-steel anode wire and a hypodermic tubing cathode. The small anode diameter minimizes avalanche fluctuations, enhancing energy resolution. Windowless flow counters use entrance windows made of materials that attenuate X-rays and alpha particles, making them ideal for detecting neutrons and low-energy radiation. Pancake detectors, with small gas volumes and multiple anode wires, are compact and effective for detecting alpha and beta particles or counting multiple radiation sources simultaneously. Finally, 4π detectors feature active surfaces on both sides, allowing them to detect particles or photons from nearly all directions, thereby increasing counting efficiency [32].

c) Fill Gas and Quenching Gas

The fill gas used in proportional counters must meet several essential criteria. It should be highly pure to avoid charge losses due to contamination and possess a low electron attachment coefficient to allow free electrons to efficiently initiate gas multiplication [32]. Monoatomic noble gases (*e.g.*, helium isotopes, argon, and xenon) are commonly utilized due to their chemical stability and high gas multiplication factors [68]. In most cases, a small amount of polyatomic gas, such as CO_2, BF_3, or CF_4, is added as a quenching gas. In some designs, these polyatomic gases may even serve as the primary fill gas without noble gas components [2, 48]. Quenching gases play a key role in suppressing unwanted signals from gamma radiation and in enhancing electron drift velocity, which improves the detector's timing resolution [57, 59]. However, the choice of quench gas also affects the neutron-gamma discrimination. While gases with higher atomic numbers (Z) are more efficient at absorbing gamma rays, they often produce fewer ion pairs, reducing the detector's overall sensitivity and discrimination capability. Specifically, xenon and argon have better performance in absorbing gamma radiation, compared to helium. This trade-off underscores the importance of gas composition optimization in detector design. [8]

d) The Output of Proportional Counters

Proportional counters typically work in pulse mode. Their main outputs include pulse amplitude and duration, which respectively reflect the number of ion pairs created and the energy of the incident radiation. These characteristics determine the timing response and energy resolution of the detector [48]. When evaluating the impacts of different gas compositions and materials, key parameters include energy resolution, timing characteristics, space charge effects, and gas multiplication factor [32].

2.2.3.3 Geiger–Müller Counters

a) Principle

As the applied voltage continues to rise beyond the proportional region, the avalanche process (previously described in the section on proportional counters) spreads along the entire anode surface, and the detector gradually loses its proportionality [48]. This phenomenon marks the onset of the Geiger-Müller (GM) region. Geiger and Müller first observed this abnormality and introduced the GM counter in 1928 [69]. These counters remain widely used today due to their advantages, including low cost, operational simplicity, and ease of maintenance [70]. GM counters are commonly employed in environmental and medical applications, such as detecting soil surface contamination, monitoring radiation in medical treatments, and routine laboratory safety checks [70]. However, they present two major limitations. First, the output pulse in GM tubes is independent of the energy of the incident radiation, as each avalanche yields a saturated and uniform pulse. This characteristic makes GM counters unsuitable for spectroscopy or energy-discriminating applications. Second, they are inefficient at high radiation intensities due to long recovery (dead) times, which lead to count losses during high-rate detection [69].

b) Geometry of GM Counters

The classic GM counter features a cylindrical geometry, though variations exist to suit specific applications. Pancake detectors provide a large detection area for enhanced efficiency, windowless designs permit high-energy beta particles to pass unimpeded, and end-window tubes are optimized for surface contamination monitoring [69].

c) Fill Gas

The fill gas requirements for GM counters are similar to those for proportional counters, as both rely on gas multiplication. Common fill gases include noble gases like neon, argon, and helium, typically at low pressures. To prevent secondary discharges, quenching gases are added at concentrations of 5–10%. Organic quenching agents (*e.g.*, ethyl alcohol and ethyl formates) are

widely used, but have limited detector lifetimes of about 10^9 counts. In contrast, halogen-based quench gases (*e.g.*, chlorine and bromine) are more durable and suitable for high-count-rate applications [32].

d) Outputs of Geiger–Müller Counters

One of the outputs of GM counters is the time characteristic, which includes rise time, dead time, resolution time, and recovery time, as shown in Figure 14. Specifically, dead time is particularly interesting to measure because it records the time interval between an initial discharge pulse and the moment when the counter is ready to detect the next event [71]. This period, ranging from tens to hundreds of microseconds, constrains the maximum count rate and can be used to analyze neutron interaction behavior [71, 72].

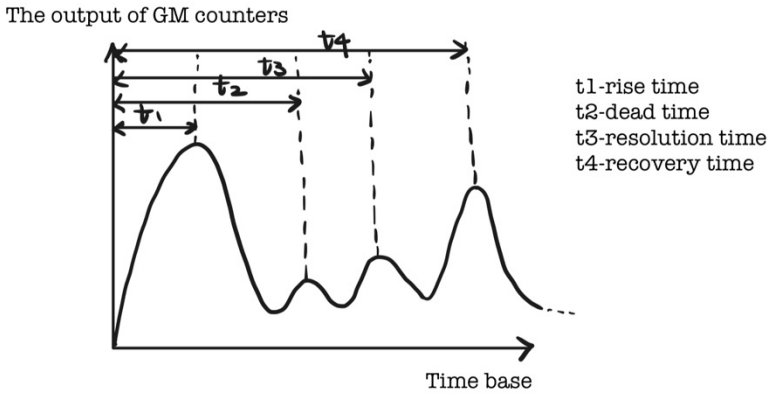

Figure 14. Time characteristics in GM tubes. The figure is adapted from [71].

Further performance insights can be obtained from the counting curve, which plots count rate versus applied voltage, as shown in Figure 15. The ideal operating voltage is typically set about one-third into the plateau region, where stability and accuracy are maximized [72].

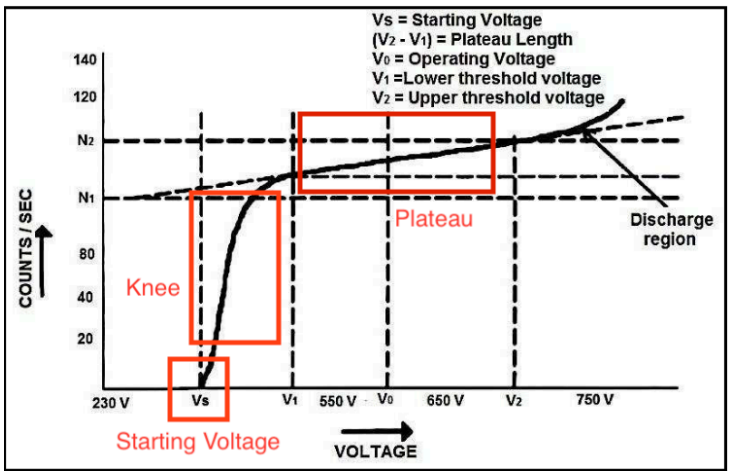

Figure 15. The Geiger counting curves as a function of applied voltage. The key operating regions, including the starting voltage, knee, and plateau, are labeled. The figure is adapted from [71].

The key regions in the Geiger counting curve are:

- Starting voltage (V_s): The minimum voltage at which detectable pulses are first registered.
- Knee (V_s-V_1): The point where the count rate begins to rise sharply with increasing voltage.
- Plateau (V_1-V_2): The region where the count rate remains nearly constant, indicating stable detector operation [32].

2.2.4 Scintillator Detectors

2.2.4.1 Introduction

a) Definition and Principles

Scintillation refers to the brief flashes of light emitted by scintillator materials when exposed to ionizing radiation [72]. This process is fundamental to many neutron detection systems and can be divided into two primary stages [32, 73]:

1. Conversion of ionizing radiation into visible or near-ultraviolet photons through luminescence within the scintillator material.

2. Conversion of these photons into electrical signals using a photodetector, typically a photomultiplier tube (PMT).

In the first stage, the scintillation mechanism differs depending on the material type, which is broadly categorized as either organic or inorganic [74]. In organic scintillators, light emission is governed by prompt fluorescence that occurs in a short time after excitation [32]. Energy from the incoming radiation excites π-electrons in organic molecules, which then relax from excited electronic states to lower vibrational states, emitting light in the process [75]. In inorganic scintillators, which often contain crystalline materials doped with luminescent ions, the radiation produces electron-hole pairs. These carriers transfer energy to dopant ions (activators), which emit photons as they return from excited states to their ground vibrational states [74, 76]. Following photon emission, the second stage involves photon-to-electron conversion and signal amplification by a PMT. This process includes the following steps [32]:

1. Incident photons strike the photocathode, releasing photoelectrons via the photoelectric effect.
2. These photoelectrons are accelerated toward the first dynode (the electrodes in the PMT tubes) by an electric potential.
3. Upon striking the dynode, each photoelectron releases additional secondary electrons.
4. This cascade amplification continues through multiple dynodes, a process known as electron multiplication.

Ultimately, the amplified electron signal reaches the final dynode and produces a measurable voltage pulse. This output is then processed by external electronics such as a linear pulse amplifier, photodiode, or avalanche photodiode for data acquisition. Different types of

scintillators are shown in Figures 16(a) and 16(b). In addition, a visual representation of the entire scintillation detection process is provided in Figure 16(c).

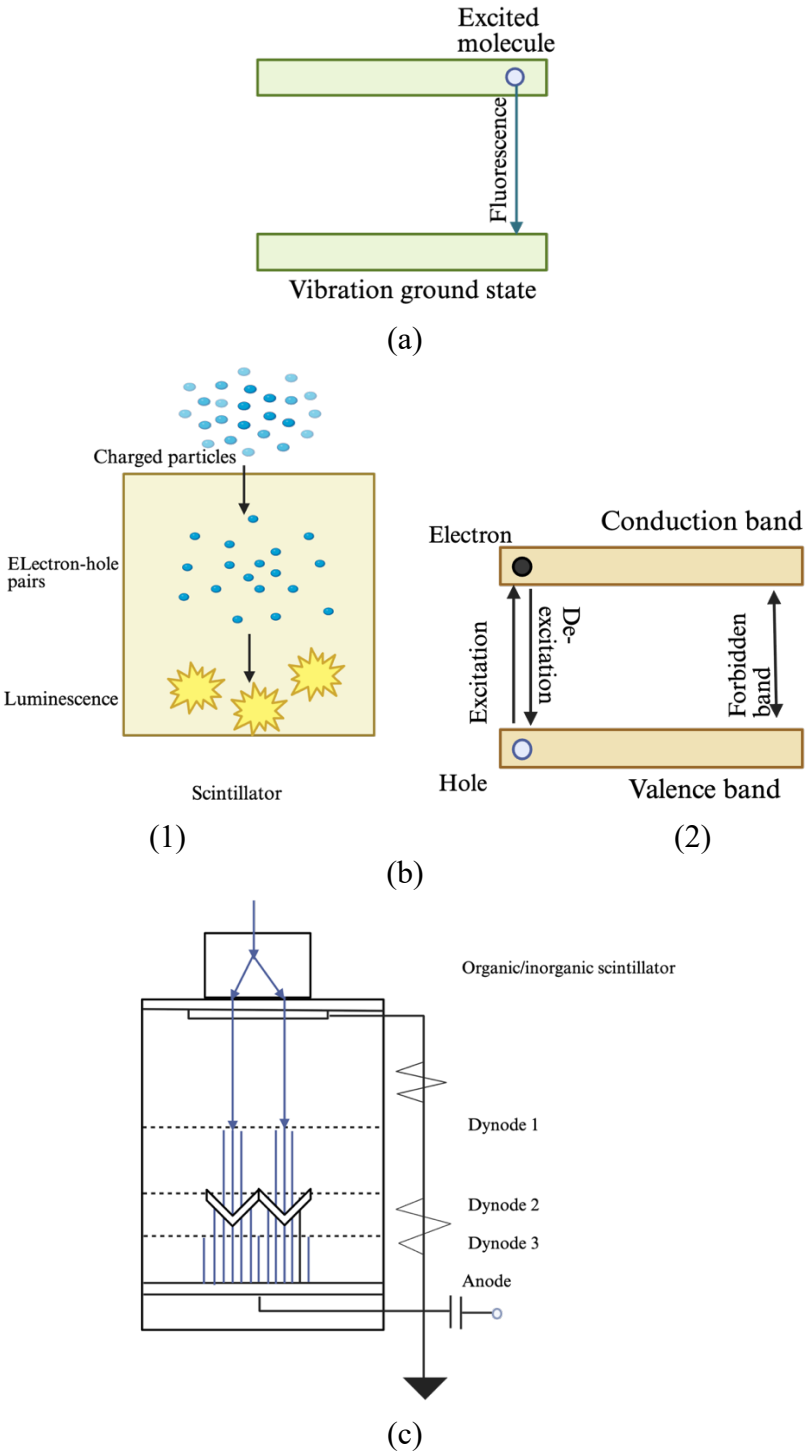

Figure 16. Schematic illustration of (a) the organic and (b) inorganic scintillators: (1) the general process in inorganic scintillators; (2) a detailed process, and (c) the process in the photomultiplier. The figures are created by the author, based on the description from [32, 77].

b) Operation Modes of Scintillators

Scintillators primarily operate in two modes, pulse mode and current mode, each producing distinct signal outputs suited to different applications. In pulse mode, scintillators generate discrete, randomly occurring pulses resulting from prompt luminescence, where light is emitted almost immediately following excitation. This mode is commonly used in applications such as nuclear medicine, where individual radiation events must be resolved. In contrast, current mode involves the production of a continuous signal proportional to the total light yield over time. This mode is typically applied in fluoroscopy and X-ray computed tomography [32]. However, under rapidly fluctuating radiation intensities, scintillators in current mode may exhibit afterglow, a residual luminescence that persists after the radiation source is removed [77].

c) Outputs and Characteristics of Scintillator Detectors

One of the most critical performance metrics of a scintillator is its light yield, defined as the number of photons emitted per unit of absorbed energy. This characteristic directly influences the signal strength and energy resolution of the detector. Although scintillator detectors do not convert all deposited energy into light, the light yield remains proportional to the energy absorbed, which determines the precision with which the incident radiation energy can be measured [32, 73]. Theoretical models, such as those developed by Davison, can be used to estimate light yield by incorporating parameters such as the mean energy required to create an electron-hole pair, the average photon energy, together with other related quantities [78].

Another key characteristic of scintillators is their decay time, which refers to the time interval during which photons are emitted after radiation interaction. A longer decay time is often desirable in pulse mode to distinguish individual events clearly [73]. Decay time is influenced by additional phenomena such as delayed fluorescence, phosphorescence, afterglow, and multi-

component luminescent states. In organic scintillators, decay time is typically short due to dominant prompt fluorescence. In inorganic scintillators, decay time can be longer, especially when involving multiple emission components or energy transfer processes [32]. Other essential characteristics include scintillation efficiency (the effectiveness of converting deposited energy into light) and emission spectrum, which describes the wavelength and intensity distribution of the emitted photons [74].

d) Pulse-Shape Discrimination (PSD)

Despite the typically short decay time of organic scintillators, many of them exhibit a delayed light component, often referred to as the slow component. This delayed emission forms the basis of Pulse-Shape Discrimination (PSD), a technique that differentiates radiation types based on variations in pulse shape [74, 76]. Different particles, including alpha particles, neutrons, and gamma photons, produce varying intensities of fast and slow scintillation components, which can be distinguished using PSD [32]. In addition to neutron and gamma discrimination, PSD is widely employed for X-ray detection in phoswich detectors (composed of two or multiple materials), particle differentiation in organic stilbene scintillator [79, 80], as well as light yield estimation [81].

e) Considerations and General Properties of Materials

Materials selection plays a critical role in optimizing the scintillation process, overall detector performance, and measurement accuracy [82]. Selecting an appropriate scintillator material involves balancing multiple interrelated properties to ensure high sensitivity, efficiency, and stability across applications. A well-performing scintillator material should achieve an optimal balance among neutron capture efficiency, light yield, energy/time/spatial resolution, afterglow behavior, and timing characteristics. Afterglow refers to the persistent emission of light after the

radiation source has been removed, which can interfere with signal accuracy in high-speed or low-background measurements [77]. To enhance light-to-electric conversion efficiency, materials with a refractive index near 1.5 are preferred, as they facilitate better coupling with photodetectors and maximize photon collection. Properties such as energy resolution, timing response, and spatial resolution directly influence the detector's ability to measure radiation with minimal noise or interference [32].

Beyond performance-specific parameters, several practical material properties must also be considered. For example, chemical stability and radiation hardness are essential to ensure long-term durability in harsh radiation environments. Scintillators must possess intrinsic or extrinsic luminescence centers capable of emitting stable light output and maintaining reliable charge states. Materials should exhibit optical transparency at the emission wavelength to facilitate efficient internal light propagation and collection. Economic viability is also important, materials should be cost-efficient and amenable to large-scale, uniform production [32, 39]. Additionally, materials with a short decay time support faster signal processing, while those with high neutron interaction cross sections or optimized interaction path lengths improve neutron capture efficiency [32].

It is important to note that the optimal properties of scintillator materials are application-specific, and performance varies significantly depending on whether the material is organic or inorganic in nature. As discussed in previous sections, these two material classes differ in their light emission mechanisms, energy resolution, decay behavior, and radiation interaction modes. The next section will provide a comparative overview of traditional organic and inorganic scintillator materials, including their performance characteristics, advantages, applications, and limitations.

2.2.4.2 Organic Scintillators

a) ***Common Materials***

Organic scintillator materials are typically composed of low atomic number elements, such as hydrogen, carbon, oxygen, and are often transparent to their own emission light [81, 83]. These materials are known for their fast response, ease of fabrication, and flexibility in geometry, making them suitable for a wide range of detector configurations. Due to their hydrogen content, organic scintillators are particularly sensitive to fast neutrons, as they rely on recoil proton detection for neutron interaction [76, 81].

b) ***Crystalline Organic Scintillators***

Among organic scintillators, anthracene is a widely used crystalline material known for its high scintillation efficiency and blue fluorescence [75, 84]. It is often used as a reference material due to its superior light yield, reported to be approximately 20,100 photons/MeV [81]. Another prominent organic crystal is stilbene, which emits light at around 350 nm and demonstrates excellent pulse shape discrimination (PSD) capabilities [75]. This material is useful in neutron and gamma separation and portable security devices [84]. Although stilbene's light yield (~16,000 photons/MeV) is slightly lower than that of anthracene, its superior discrimination properties and geometric flexibility contribute to its practical appeal [81]. Both materials are also employed in neutron imaging, where spatial variations in light yield across the crystal surface enable position-dependent measurements [84]. Beyond traditional crystals, fluorescence materials that show aggregation-induced emission (AIE) have emerged as promising candidates, offering acceptable light yields with enhanced design flexibility [81].

c) ***Organic Liquid Scintillators***

To address the cost and scalability limitations of crystal scintillators, organic liquid scintillators are widely adopted for their cost-effectiveness, chemical stability, non-toxicity, and competitive light yield (often exceeding 19,000 photons/MeV) [76, 84, 85]. These liquids are used in applications such as low-energy neutron detection, biological radiotracking, and radioactive contamination analysis. Common solvents include toluene and xylene, as well as modern alternatives such as linear alkylbenzene (LAB) and phenyl-o-xylylethane (PXE). Recently, π-conjugated solvents have attracted interest for their adequate light yield and capability to function without fluorescent dopants [81].

d) ***Polymeric (Plastic) Organic Scintillators***

Polymeric scintillators play a major role in plastic scintillator applications, offering advantages in mechanical strength, processing, and flexibility. Conventional materials such as polyvinyltoluene (PVT) and polystyrene (PS) have been widely used, but modern polysiloxane-based materials are gaining attention due to their superior properties [81]. For example, phenyl-polysiloxane scintillators demonstrate improved radiation resistance, thermal stability, PSD performance, and neutron/gamma discrimination, making them well-suited for harsh radiation environments [55, 81]. In addition, new organic fluorescent compounds with thermally activated delayed fluorescence (TADF) and AIE characteristics show promise due to their unique photophysical properties and solubility, facilitating novel scintillator designs [81]. However, one limitation of polymeric scintillators is their susceptibility to radiation-induced degradation, which can diminish light output over time [32].

2.2.4.3 Inorganic Scintillators

a) ***Common Materials***

Unlike organic scintillators, inorganic scintillators are composed of high atomic number (Z) elements, making them particularly effective for gamma-ray detection due to their superior photon absorption capability [74]. These materials typically exhibit a higher light yield and greater stopping power than their organic counterparts. They are commonly fabricated as large single crystals or ceramic plates, requiring high purity and crystallinity to ensure efficient scintillation performance [76]. However, pure inorganic crystals often have bandgaps too large to effectively emit photons via direct excitation. To overcome this limitation, dopants, commonly referred to as activators, are introduced into the crystal lattice. As illustrated in Figure 17, these activators create intermediate energy levels within the bandgap, enabling efficient radiative transitions and significantly enhancing scintillation efficiency [74]. Typical activators include transition metals or rare-earth elements, especially those with an s^2 outer electron configuration (Eu^{2+}, Ce^{3+}, Sm^{2+}, and Ag^{+}), which form effective luminescent centers [77]. For example, activators such as Th, Sn, or Ag are preferred for high-count-rate neutron detection due to their short decay times. In contrast, Eu and Sm are used when high light output and good optical transparency are priorities [67, 86]. Other applications of inorganic scintillators include high- and low-energy physics (such as calorimeters), medical imaging systems (such as computed tomography), gamma radiation cameras, as well as neutron detection systems [39, 76].

In addition, thermal simulation provides supplementary energy to excite and de-excite electrons at higher energy levels for effective light emission. This method is commonly seen in doped materials where radiative transitions to the ground state are forbidden. Simultaneously, the

resulting slow luminescence components are referred to as phosphorescence, which contributes to afterglow, a persistent light signal following radiation exposure [32].

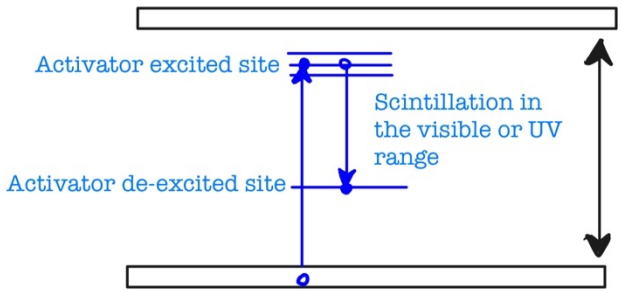

Figure 17. Schematic diagram showing the creation of luminescence centers by incorporating activator ions into the host lattice. The figure is created by the author, based on the description from [82].

To enable thermal neutron detection, isotopes like ^{10}B and ^{6}Li are incorporated into the lattice. These nuclei participate in exothermic nuclear reactions:

$^{10}B(n, \alpha)^{7}Li$;

$^{6}Li(n, \alpha)^{3}H$ [39, 87]

In the case of ^{6}Li, the reaction produces tritium (^{3}H) and an alpha particle (^{4}He), which then excite luminescent centers and generate electron-hole pairs, initiating the scintillation process [87]. These reactions are highly favorable due to their large thermal neutron cross-sections and high Q-values, making such materials ideal for low-energy neutron detection [77].

One of the most well-known inorganic scintillators is thallium-doped sodium iodide (NaI:Tl). It offers a very high light output of up to 38,000 photons per MeV, making it a benchmark scintillator [74]. However, its long decay time (~230 ns) and phosphorescence, about 9% delayed emission, limits its use to high-rate environments. NaI(Tl) is also widely used in applications such as uranium enrichment monitoring, where sodium and fluorine in UF_6 react with uranium to emit alpha particles, and the neutron signal correlates with uranium content [88]. In addition, lithium

iodide (LiI), discovered by Hofstadter in 1948, has a similar structure and scintillation behavior to NaI(Tl), but with distinct advantages for neutron detection. It offers low gamma sensitivity, high thermal neutron cross-section (870–940 barns), and a Q-value of 4.78 MeV, making it ideal for thermal neutron applications [86, 87].

Several other inorganic materials display different scintillator characteristics, tailored for various uses (see Table 5). For example, bismuth germanite ($Bi_4Ge_3O_{12}$, or BGO) is a non-alkali scintillator with high density, suitable for positron emission tomography (PET) due to its excellent gamma-ray absorption [89]. In addition to BGO, lithium glass scintillators offer good neutron/gamma discrimination, moderate cost, and are used as an alternative to helium-3 detectors in thermal neutron multiplicity measurements [90].

Beyond these material-specific properties, scintillators also differ in timing behavior. Inorganic scintillators typically exhibit decay times ranging from 30 to 500 nanoseconds, depending on material composition and dopant levels. Some materials follow a single exponential decay, while others exhibit multiple decay components, affecting time resolution. Comprehensive performance data (for example, light yield, decay time, and energy resolution) has been systematically compiled by Knoll and remains a standard reference for scintillator evaluation [32].

Table 5. Scintillation characteristics of inorganic scintillator materials. The table is created by the author and the data is provided from the references provided within the table. N/A means that the values have not been found from currently available studies.

Material	Advantages	Scintillation efficiency (%)	Density (g/cm^3)	Decay time (ns)	Light yield photons per MeV from gamma	Emission peak (nm)
NaI (Tl)	As a standard; high light output	11.3 [91]	3.7 [38]	230 [88]	38,000 [88]	415 [91]
LiI (Tl)	Fast decay time	N/A	4.1 [2]	(180±18 ns) [87]	14,000 [87]	N/A
LiI (Eu)	Transparent to the scintillation light and high light output	N/A	4.1 [92]	1200 [87]	15,000 [87]	470 [92]
Li glass	Transparent to the scintillation light	2.8 vol [90]	2.5 [92]	75-100 [87]	4,000 [87]	395 [92]
LiF/ZnS:Ag	Performance varies from compositions	26.4	2.6 [92]	100 [92]	75,000 [83]	~450 [92]
$LaBr_3$ (Ce)	High density; High light yield; good timing characteristics	N/A	5.3 [89]	35 [89]	61,000 [89]	358 [89]

2.2.5. Semiconductor Detectors

2.2.5.1 Principles and Configurations

With the rapid advancement of semiconductor fabrication technology, semiconductor detectors have garnered increasing attention since the early 1960s. These detectors belong to the class of solid-state radiation sensors, and their underlying detection mechanism shares similarities

with inorganic scintillators, particularly in the process of charge generation and collection. When ionizing radiation or charged particles interact with a semiconductor material, they deposit energy into the medium, exciting electrons from the valence band into the conduction band and thereby creating electron–hole pairs [32]. The number of charge carriers generated is proportional to the energy deposited. By applying an external electric field, these carriers are collected at the electrodes, resulting in a measurable electrical pulse [93]. The pulse-height spectrum, a distribution of pulse amplitudes, is used to extract information such as radiation energy, event counts, and energy resolution.

Semiconductor detectors are typically fabricated with a compact, planar geometry, often realized in the form of p–n junction diodes or Schottky junctions. Figure 18 shows the typical configuration of a semiconductor detector. To enable neutron detection, the surface of the detector is often coated with neutron-reactive materials such as boron-10 (^{10}B) or lithium fluoride (^{6}LiF) [2, 38, 94]. These materials undergo ^{10}B (n, α)^{7}Li and ^{6}Li (n,t)^{4}He nuclear reactions upon interaction with thermal neutrons. Both reactions release energetic charged particles (α or ^{3}H), which subsequently generate electron–hole pairs within the semiconductor substrate, initiating the detection process. Due to their high neutron cross-sections, these coatings are highly effective in enhancing thermal neutron sensitivity. Additionally, the layered design of these detectors helps to reduce leakage current and minimize electronic noise, both of which are crucial for achieving high signal-to-noise ratios and maintaining detector stability over time [2].

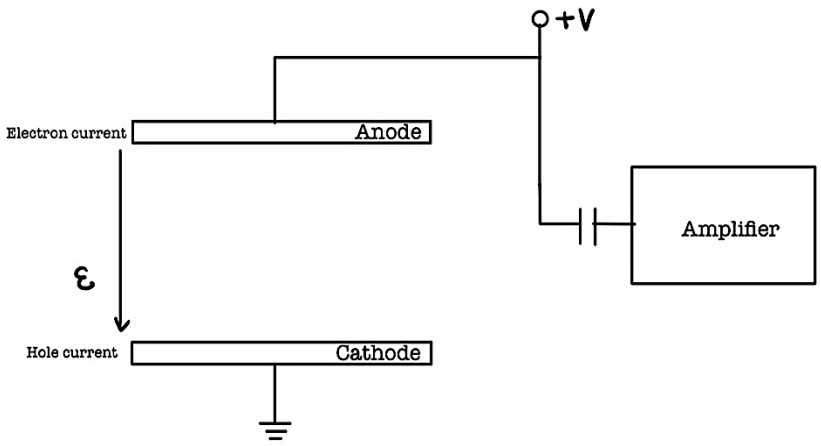

Figure 18. The configuration of semiconductor detectors. The figure is adapted from [94].

2.2.5.2 Material Properties

Achieving optimal performance in semiconductor detectors requires the generation of a sufficient number of electron–hole pairs to produce strong, reliable signals. To enable this, semiconductor materials must possess several key physical and electronic properties, outlined below.

a) Electrical Properties and Doping Behavior

The electrical behavior of semiconductors is highly sensitive to variations in crystal purity and doping. These changes can be intentional (extrinsic doping) or unintentional (intrinsic defects), both of which affect the carrier concentration and transport properties [32, 93]. In extrinsic semiconductors, dopant atoms are introduced into the crystal lattice, acting as donors or acceptors depending on the electronic structure. Specifically, donor doping refers to adding Group V elements (for example, phosphorus, arsenic) to Group IV semiconductors (for example, silicon), contributing extra electrons and resulting in n-type conductivity. Group II elements (such as zinc), with Group IV elements, can also act as donors but introduce deeper energy levels. In contrast, the acceptor doping involves adding Group III elements (for example, boron) to create holes by

capturing electrons, leading to p-type conductivity [93]. The depth of these dopants in the energy gap, whether shallow or deep, determines how easily charge carriers can be excited. Additionally, intrinsic materials can be affected by contamination or defect formation during crystal growth, polishing, or radiation exposure, altering the balance of free carriers [32].

b) Bandgap Energy

The bandgap is the minimum energy required to generate an electron–hole pair [95]. For efficient detection, a bandgap around 1.2 eV is minimal to allow many charged carriers to be produced per unit of absorbed radiation energy [93], [96]. Wider bandgaps (*e.g.*, 2–6 eV) are also desirable for low leakage currents, reduced electronic noise, and room-temperature operation [97]. Larger bandgaps are frequently found in compound semiconductors than elemental crystals, improving thermal stability and noise suppression [94].

c) Density and Charge Collection Efficiency

Semiconductors with high density (typically >2.3 g/cm^3) and thin geometries can produce large signals. However, in such dense materials, carrier mobility can remain high to prevent recombination and allow efficient charge collection before trapping occurs [93].

d) Crystalline Purity and Structural Integrity

High-purity, defect-free crystals facilitate free movement of carriers and reduce signal degradation due to trapping. This improves charge collection efficiency and resolution [38, 93]. Despite advancements, producing ultra-pure crystals remains a significant challenge.

e) Influence of Applied Voltage

The electron collection efficiency (ECE) is directly affected by the applied voltage. For many semiconductors, ECE increases proportionally with voltage, as stronger fields enhance carrier drift and suppress recombination losses [96].

f) Mechanical, Thermal, and Radiation Stability

Given their use in extreme environments, semiconductor materials must be mechanically robust and resistant to gamma radiation-induced degradation [93, 96]. Doping can increase defect formation energy, improving both radiation hardness and mechanical durability [94]. Additionally, temperature rises during operation due to heat from radiation absorption. Thus, thermal conductivity becomes critical. Materials with high thermal conductivity (*e.g.*, diamond) are more effective at dissipating heat, preserving detector performance under thermal stress [98].

2.2.5.3 Traditional Semiconductor Detector Materials

Elemental semiconductor detectors are commonly fabricated using signal crystals such as diamond, silicon, and germanium due to their favorable charge transport properties, bandgap energies, and radiation interaction mechanisms [38, 45, 99]. For example, diamond is a wide bandgap material (5.5 eV) that offers exceptional radiation hardness, high thermal conductivity, and a high melting point, making it suitable for fast neutron spectroscopy and operation in high-temperature environments [96, 99]. In diamond-based neutron detectors, the $^{12}C(n, \alpha)^{9}Be$ reaction is typically utilized for monoenergetic neutron detection [99]. In addition to diamond, silicon is widely used in charged particle detection due to its established fabrication technology and high-resolution performance. Its neutron interaction is governed primarily by the ^{28}Si (n, alpha) and ^{28}Si (n, p) reactions. Silicon detectors are particularly advantageous for integration with electronics and are widely used in both scientific instrumentation and commercial applications [93, 99]. In addition,

high-purity germanium (HPGe) has been studied since the 1970s, particularly in gamma-ray spectrometry, X-ray detection, and near-infrared applications due to the small bandgap (~0.66 eV) and the requirement of cooling to liquid nitrogen temperatures [38, 93].

Beyond elemental semiconductors, compound semiconductors provide increased design flexibility and performance. They are widely used in high-resolution gamma spectrometry and high-radiation environments [38]. These materials offer several advantages: (a) broader bandgap range, (b) higher atomic numbers and densities, (c) higher stopping power at or near room temperature, resulting in thinner detectors and radiation resistance, and (d) tunable compositions, enabling lattice constants and bandgap energy customization [94].

A prominent example of compound semiconductors used in semiconductor detectors is cadmium telluride (CdTe) doped with zinc. Specifically, cubic Zn-doped CdTe has been one of the most widely adopted compound semiconductors since the 1960s. It combines a large bandgap, high resistivity, and low defect density, resulting in low leakage current and stable operation at elevated temperatures, ideal for portable spectrometry and space applications [38, 94]. Table 6 summarizes key physical and electronic properties of selected semiconductor materials, including bandgap energy, density, carrier mobility, thermal conductivity, radiation resistance, and energy resolution. These parameters are critical for selecting suitable materials for specific detection environments and applications.

Table 6. Characteristics and performance of common semiconductor materials. The table is created by the author and the data is provided from the references within the table. N/A means that the values have not been found from currently available studies.

Material	**Band gap energy (eV)**	**Density (g/cm^3)**	**Electron/hole mobility ($cm^2/(V·s)$)**	**Thermal conductivity [W/cm·K]**	**Resistivity (Ω*cm)**	**Energy resolution at room temperature**
Diamond	5.5 [96]	3.52 [93]	Electron: 1800 Hole: ~1200 [93]	~10 [93]	N/A	3.5 % [96]
Si (Z=14)	1.12 [93]	2.33 [93]	Electron: 1450-1500 Hole: 450-505	~1.5 [93]	$230* 10^3$ [93]	N/A
Ge (Z=32)	0.66 [95] or 1.57 [94]	5.32 [93]	Electron: 3900 Hole: 1800-1900	0.6 [93]	47 [93]	< 0.2% [38]
GaAs	1.42 [94]	5.32 [100]	Electron: 8500 Hole: 400 [97]	0.45 [93]	10^8 [97]	30-40% [97]
$Cd_{1-x}Zn_xTe$	1.6-2.4 [97]	5.7-6.2 [97]	Electron: 1120 Hole: 200 [97]	N/A	10^{11} [84, 97]	7-8% [97]
HgI_2	2.13 eV (below 403 K) 2.5 eV (above) [94]	6.4 [97]	Electron: 100 Hole: 4 [97]	N/A	10^{14} [97]	1-6% [97]

2.2.5.4 Advantages, Disadvantages, and Applications of Semiconductor Detector Materials

Although semiconductor detectors generally have lower neutron detection efficiency than gaseous and scintillator-based detectors, they offer several distinct advantages that make them well-suited for specific applications [96]. One key advantage is their fast response time and intrinsic insensitivity to environmental noise, which enables reliable neutron detection even in extreme conditions such as high temperatures or strong electromagnetic fields [96]. In addition, because they do not require the conversion of energy into light, unlike scintillators, semiconductor detectors provide superior energy resolution, allowing for more precise measurements of the energy and identity of interacting charged particles [2]. Their compact size and high material density also contribute to their capability in detecting high-energy electrons and gamma radiation, making them versatile across a range of radiation detection tasks. Table 7 provides a comparative summary of the advantages, applications, and limitations of semiconductor detector materials [32, 38].

Table 7. Applications, advantages, and limitations of semiconductor detector materials.

Semiconductor Detector Materials	Advantages	Applications	Limitations
	Better resolution	Security	Expensive
	High density	High-purity electrons and X-ray detection	Less efficient and difficult in operating due to small sizes
	Small size		Demanding synthetic conditions for flawless crystals
	Insensitivity to gamma radiation	Gamma radiation detection	Elevated sensitivity to performance degradation from radiation-induced damage

Chapter III. Study of Hydroxyapatite in Dosimetry for an Improved Portable Personnel Neutron Radiation Protection

3.1. Introduction

Through neutron detection, researchers have established that neutrons interact with matter to produce ionizing radiation. This radiation has biological effects once the absorbed dose exceeds established thresholds. Traditionally, acceptable neutron radiation dose limits range from 10 to 156 rad [101]. Various international agencies have defined radiation safety standards. For example, the U.S. Environmental Protection Agency states that doses over 0.75 Gray (Gy) can cause acute radiation syndrome, and the European Directive limits occupational exposure to 20 mSv per year [102]. The unit conversion of the absorbed dose is 1 Gy = 100 rad = 1 J/kg. For dose equivalence that accounts for biological effects, 1 Sievert (Sv) = 100 rem [32]. The unit rem expresses the biological effectiveness of radiation in human tissue. For diagnostic purposes, it is numerically equivalent to rad, which quantifies the actual energy absorbed by local tissues [103].

In addition to biological effects, ionizing radiation can degrade detector performance and reduce material lifetime. For example, organic scintillators are susceptible to polymer degradation under high-dose radiation exposure. Meanwhile, the extent of radiation damage varies depending on dose, dose rate, radiation type, and particle energy. For instance, thallium-activated alkali halide scintillators exhibit damage effects starting at 10 Gy, whereas $LaBr_3$-based scintillators typically withstand up to 1,000 Gy before damage becomes apparent [32].

Thus, the development of radiation-resistant materials is essential for accurate dose measurement and for ensuring that exposure remains within safe and effective limits, particularly in medical applications like radiotherapy. The following chapter explores historical and emerging materials in neutron dosimetry and proposes hydroxyapatite as a portable dosimeter to assess the

absorbed doses. Portable dosimeters can also be useful in routine health screening and radiation monitoring for the general population [104].

3.2 Radiation Dosimetry Systems

Radiation dosimetry refers to the measurement, calculation, and assessment of the ionizing radiation absorbed by a medium, most commonly, the human body. For example, tooth enamel can be used in electron spin resonance dosimetry (ESD) [105]. A dosimetry system consists of a dosimeter, which undergoes physical or chemical changes when exposed to radiation, and a reader that quantifies those changes to calculate the absorbed dose. Dosimeters are categorized based on the type of changes they record, including [102], color change, temperature rise, and ionization level. To quantify radiation-induced chemical signals, methods such as titration, ultraviolet spectroscopy, and electron paramagnetic resonance (EPR) are used. Modern science employs four main types of dosimeters with various working principles [106, 107]:

- Luminescence dosimeters
- Film dosimeters
- Semiconductor dosimeters
- Ionization chamber dosimeters

Table 8 summarizes the applications and representative materials for each type.

3.3. Luminescence Dosimeters

Luminescence dosimeters, conceptually similar to scintillation detectors, detect ionizing radiation by converting stored energy into light, which is then transformed into electrical signals [106]. However, they differ significantly from scintillators in principles, applications, and material composition. Unlike scintillation detectors, luminescence dosimeters rely on phosphorescence processes, and their active materials are referred to as phosphors. Depending on the stimulation

method of releasing stored energy, two common luminescence dosimeters include thermoluminescent (TL) and optical stimulated luminescence (OSL) dosimeters [108]. Upon exposure to ionizing radiation, energy is absorbed by the phosphor material, causing electrons to become excited and transition to the conduction band. These electrons become trapped at defect sites within the material's band structure [109]. Later, these excited electrons return to their ground state when stimulated, either by light at a specific wavelength (typically from a laser) or by heat (usually between 200°C and 400°C), resulting in the emission of visible light or infrared radiation, respectively. Subsequently, this emitted light, or radiation is then converted into measurable electrical signals in the charge or current form, typically using a photomultiplier tube (PMT) [106]. As illustrated in Figure 19, the working principle of OSL and TL dosimeters is defined.

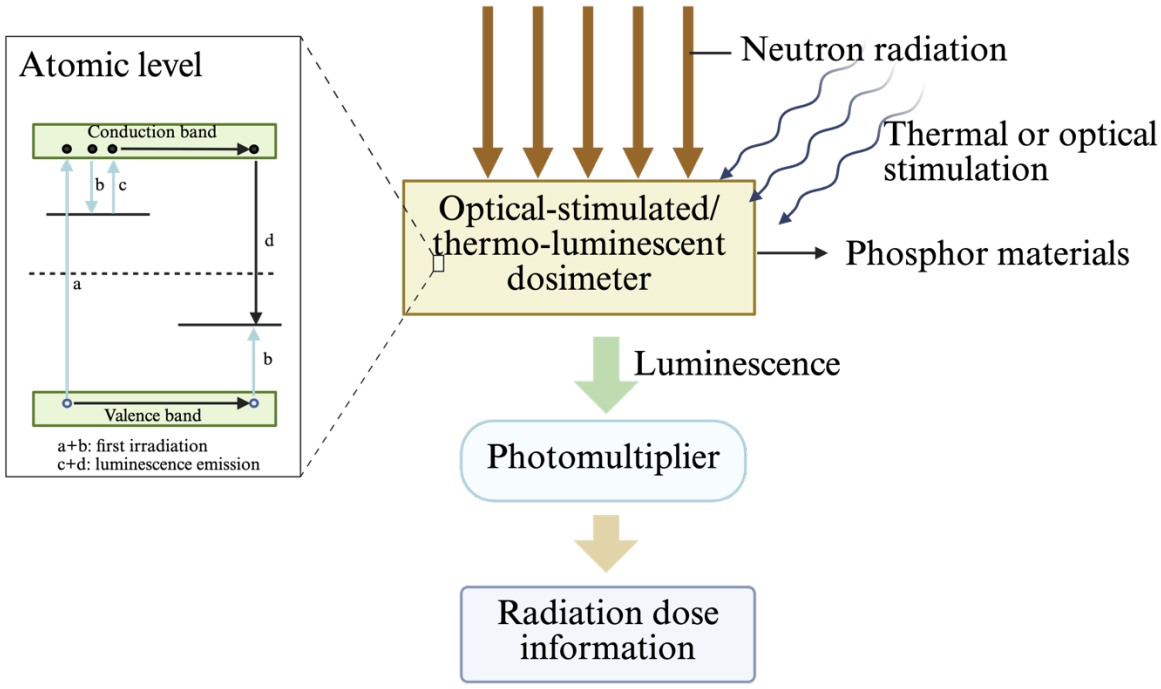

Figure 19. Schematic illustration of the working principle of TL and OSL dosimeters. The figure is adapted from Bos [110] and Nikaido [111].

Thermoluminescent dosimeters (TL) were discovered in the 19th century and have since become one of the most widely studied and used tools for personnel and environmental radiation monitoring in hospitals and research institutions [104, 106, 112]. They are especially valued for their small particle sizes, flexible forms, and lack of required cables [104]. TL dosimeters are particularly widely employed in radiotherapy, *in vivo* dosimetry, and treatment technique verification [106]. In both types, the intensity of the emitted light is proportional to the radiation dose, allowing for accurate dose measurements [106, 108].

Optically stimulated luminescence dosimeters (OSLDs) were introduced in the 20th century. In OSL dosimeters, light emission is retrieved using a specific "READOUT" process [108]. OSL dosimeters offer notable advantages, such as high sensitivity, rewritable use, and non-destructive readout, making them ideal for applications [106, 108]. OSL dosimeters are often used as passive personal dosimeters, in computed radiography (CR) for medical and dental diagnostics, in environmental monitoring, *in vivo* radiation assessment, and in autoradiography for drug discovery [108]. Aside from the stimulus type (heat vs. light), OSL and TL dosimeters share many similarities, including material selection and application versatility.

Table 8. The classification of existing dosimeters. The table is created by the author based on descriptions provided in [102, 106, 111, 113].

Dosimeter type	**Classification**	**Material representative**	**Applications**
Luminescence	OSL	• Fiber Al_2O_3:C • BeO, BaBrF:Eu, Y_2SiO_5:Ce, Sm, and KBr: In	• Radiotherapy • Radiodiagnostics: *in vivo* dosimetry • Heavy charged particle dosimetry
	TL	• Tissue equivalent: LiF and $Li_2B_4O_7$	• In vivo dosimetry • Pottery dating • Radiotherapy

		• Sensitive: $CaSO_4$:Dy, Al_2O_3:C, CaF_2:Mn	• Treatment technique verifications
Film	Radiographic	Container: plastic with AgBr in gelatin	• Qualitatively and quantitatively electron beam dosimetry, quality control of radiotherapy machines
	Radiochromic	Light-sensitive polymers	• High dose gradient regions
Semiconductor	Silicon diode	n- and p-type Si	• p-type Si for radiotherapy due to its radiation resistance and smaller dark current • Measurements in phantoms • *In vivo* dosimetry
	Metal-oxide semiconductor field effect transistor (MOSFET)	Metal oxide	• *In vivo* dosimetry • Threshold voltage measurements • Routine patient dose verification • Radiosurgery • Brachytherapy
Ionization Chamber	Cylindrical	Wall: low atomic number materials Electrode: Al	• Beam calibration in radiotherapy
	Plane-parallel	Wall: non-conducting materials (polystyrene) Electrode: graphite	• Dosimetry of electron beam with energy lower than 10 keV • Surface dose and depth dose measurements of megavoltage photon beams
	Brachytherapy		• Clinical use
	Extrapolation		• β-ray and low energy X-ray dosimetry • Absolute radiation dosimetry

			• Surface doses in ortho- and mega-voltage X-ray beam
Other	Electron paramagnetic resonance	Alanine	• High dose dosimetry • Precise radiotherapy dosimetry at the level of above 10 Gy
	Plastic scintillator		• Brachytherapy • Ophthalmic plaque dosimetry • External beam dosimetry
	Diamond	Natural diamond Container: polystyrene Contacts: Au	• Radiosurgery
	Gel	• Fricke gels (ferrous sulphate in gelatin, agarose, or PVA) • Polymer gels (acrylamid in gelatin or agarose)	• Fricke: 3 dimensional images of the dose distribution • Polymer: NMR, X-ray computed tomography (CT), optical tomography, ultrasound spectroscopy

3.4 Material Properties for Luminescence Dosimeters (OSL and TL Dosimeters)

Selecting appropriate materials is essential for the optimal performance of dosimeters. The choice of material directly influences critical performance factors such as accuracy, precision, linearity, dose/dose-rate dependence, tissue equivalence, and size [106, 114]. While some general criteria apply to all dosimeters, specific material requirements depend on the type of dosimeter and its operational principle. In luminescence dosimeters, phosphor materials are widely used due to their favorable optical characteristics. Below is a summary of key properties required for OSL (optically stimulated luminescence) and TL (thermoluminescence) dosimeters [112].

a) Low fading

Thermal fading refers to the reduction of luminescence intensity caused by temperature changes [109]. In luminescence dosimeters, charge carriers (electrons or holes) created by radiation are trapped in defect sites within the material, which store dose information. A low thermal fading ensures that these carriers remain trapped until readout. F-centers, common in TL materials, are defect sites that stabilize trapped carriers for extended periods, thereby minimizing signal loss [112]. The information about fading can be achieved through the diagram of relative TL intensity over time. The flatter the line is, the lower the fading is.

b) Dose and energy response

Materials must exhibit linear luminescence intensity over a wide range of absorbed doses [105, 112]. This relationship is typically visualized in the glow curve of TL dosimeters, which plots luminescence emission intensity over time or temperature. A well-defined peak (for traditional materials often near 200°C) corresponds to specific trap depths [106, 109].

c) Tissue equivalence

Moreover, tissue equivalence is critical. Luminescent materials should mimic human tissue in their interaction with ionizing radiation to prevent damage to actual biological tissue. This equivalence is achieved when the material's mass energy absorption coefficient closely matches that of tissue. Materials with an atomic number value near 7.35 are generally considered tissue equivalent [104, 110].

d) High sensitivity

High sensitivity ensures a stronger signal output per absorbed dose. It is quantified as luminescence intensity per unit absorbed dose (mass or area) [110]. Sensitivity depends on various factors, including [109], the readout system, material form (powder, pellet, etc.), and radiation type and energy.

e) Other factors

In addition to optical and dosimetric properties, ideal materials should also be [109] radiation resistant, mechanically robust, chemically stable, cost-effective, and easily fabricated or synthesized. Materials must also retain signal stability over time to ensure long-term durability [105].

For TL dosimeters (TLD) associated with heat, materials also possess additional properties, such as proper emission spectra, glow curve, and reproducibility, as follows:

a) Emission spectra

Ideal materials emit light in the visible spectrum, typically between 400–500 nm, enabling visual detection and compatibility with photodetectors [109].

b) Good reproducibility

Materials must yield consistent signal outputs under identical experimental conditions to ensure reliability and repeatability of results [21].

c) Glow curve

The glow curve reflects the relationship between the normalized thermoluminescence intensity and temperature [106]. Most dosimetric materials have one main peak, indicating the highest TL intensity at a specific temperature. The glow curve is influenced by the heating rate, which affects how quickly and sharply thermoluminescence is recorded. A faster heating rate results in higher and narrower peaks, which is beneficial for parameter extraction like activation energy and kinetic order [115]. Materials with a single dominant glow peak are preferred for ease of use and simple interpretation.

d) Annealing behavior

Annealing allows the reuse of TL materials by resetting the dosimetric signal (zeroing traps). Materials should withstand repeated thermal cycles without degrading their dosimetric properties [110].

3.5. Conventional Dosimetric Materials

The most widely used materials for dosimetry are solid-state inorganic crystals, including fluorides, sulfates, oxides, and borates [47]. These are often doped to enhance their luminescent performance. LiF, whose sensitivity is often used as a reference compared to other dosimetric materials, remains one of the most commonly employed materials for personnel dosimetry. Typically doped with Mg, Ti, Cu, or P, LiF exhibits favorable response characteristics to thermal neutrons via nuclear reactions, such as $^{6}Li\ (n, \alpha) \rightarrow {}^{3}H$ and $^{10}B\ (n, \alpha) \rightarrow {}^{7}Li$ [109]. In addition to Li-containing inorganic materials, other inorganic materials exhibit excellent dosimetric characteristics, as shown in Table 9.

Table 9. The characteristics of common dosimetric materials.

Substrate material	Dopants	Effective atomic number Z_{eff}	Main peak (℃)	Emission maximum (nm)	Relative gamma ray sensitivity (a.u.)	Fading (25 ℃)	Useful dose range
LiF [109]	Mg, Ti	8.2	195	400	1	5% / year	50 μGy-10^3 Gy
$Li_2B_4O_7$ [109]	Mn	7.4	210	600	0.4	10% / month	0.1 mGy-3 Gy
	Cu	7.4	205	368	8	4.5% / month	N/A
$CaSO_4$ [116]	Dy	15.3	240	480-570	50	3 % / month	10 μGy-100 Gy
CaF_2 [109]	Dy	16.0	260	380	23	N/A	10 μGy-10^3 Gy
Al_2O_3 [117]	C	10.2	190	300, 400, 693	60	5% / year	0.3-1000 mGy

3.6. Novel Dosimetric Materials: Hydroxyapatite

Despite the broad range of established dosimetric materials, the development of novel dosimetric materials that offer maximum sustainability at minimal cost remains a critical area of research. One particularly promising candidate is hydroxyapatite (HAp), a widely studied bioceramic material that serves as the main inorganic constituent of human bones and teeth. Chemically denoted as $Ca_{10}(PO4)_6(OH)_2$ [118], HAp crystallizes in a hexagonal lattice structure with a $P6_3/m$ space group [18, 119].

3.6.1. Synthesis Methods

To achieve optimal material performance, it is essential to synthesize HAp with tailored properties by carefully controlling its composition and morphology. HAp, a widely recognized bioceramic material, is typically synthesized using heat treatment and calcination. These processes are essential for optimizing micropore size and crystallinity, narrowing the micropore size distribution, and enhancing particle size uniformity. To enhance the luminescent properties of HAp for dosimetric applications, doping, particularly with lanthanide elements, has become a widely adopted strategy. In this section, several synthesis routes for obtaining HAp are presented (see Table 10), and the dosimetric performance of HAp, both doped and undoped, is evaluated and compared.

Table 10. Synthesis routes of HAp, precursors, conditions, and additional operations.

Synthesis method	Precursors	Conditions	Notes
Hydrothermal	$Ca_{9.4}H_{0.6}(PO_4)_6(OH)_{1.4}•4H_2O$, $Ca(OH)_2$ [119]	T = 973 K, P = 750 bar, 72 h	
Sol-gel	P_2O_5, $Ca(NO_3)_2•4H_2O$, C_2H_5OH [21, 120]	T: 1) stirring at room temperature for 1h. 2) 56°C for 14 h, stop stirring until precipitation is observed.	Calcination and pulverization required for crystallinity and structural characterization.
	P_2O_5, $Ca(NO_3)_2•4H_2O$ [121]	1) 56°C for 48 h 2) Calcination temperature: 600-1200°C	Applied gamma irradiation after sintering.
Microwave	Na_3PO_4, $CaCl_2$ (ratio = 1.67) [120]	30 min, microwave power = 800W	
Hydrolysis	$CaHPO_4•4H_2O$, $Ca(OH)_2$, NaOH (ratio = 1.67) [122]	pH = 13, T = 75°C, 1 h	In a high-speed agitator.

3.6.2. Dosimetry Performance

To evaluate the thermoluminescent (TL) properties of HAp synthesized via the hydrolysis method, the material was irradiated with gamma rays from a ^{60}Co source over a dose range from 25 to 10,000 Gy at a rate of 2.71 Gy/s [123]. The experimental results demonstrate that HAp exhibits promising TL behavior across several key parameters, including fading behavior, dose response, glow curve characteristics, reproducibility, and annealing behaviors. First, based on the studies of Shafaei and Zarinfar, the TL intensity profile of HAp displays a primary peak near 200°C [22]. In addition, the fading study showed that HAp experienced faster signal degradation at low temperatures but remained stable at room temperature over a three-week period. After one month at room temperature, the total TL response decreased by 32%. Furthermore, the dose response demonstrated a linear relationship between TL intensity and absorbed doses before and after

annealing, which indicated that the properties of HAp remain unchanged and the material exhibits good annealing stability behavior. Lastly, a reproducibility value of approximately 3.5% confirmed that HAp can yield stable signal outputs under identical conditions.

Following the evaluation of the hydrolysis route, the hydrothermal method was also investigated for its potential in producing thermoluminescent HAp. In the study conducted by Lapraz [120], the glow curve revealed a weak main peak at 132 K (approximately -141.15℃), with emission spectra ranging from 350 to 600 nm, well within the typical TL detection window. The dose response in this study also followed a linear relationship with absorbed doses ranging from 10^{-5} to 0.87 Gy, based on a reported conversion from 10^{-2} to 10^{2} R (Roentgen) using standard conversion factors found online (1 R = 0.00877 Gy in air). However, no further TL characteristics, such as reproducibility or fading behavior, were detailed in this study, leaving the overall dosimetric performance of hydrothermally synthesized HAp less well understood.

In addition, Rivera-Montalvo [21] investigated the TL properties of HAp synthesized via the sol-gel method. In this study, HAp demonstrated enhanced fading resistance, with only a 9% reduction in TL signal intensity over a 90-day period, substantially lower than the 32% fading observed in the hydrolysis method and approaching the commercial benchmark of 5%. The TL response also exhibits strong linearity across a broad absorbed dose range, from 1 to 100 Gy. The emission spectra of HAp ranged from 350 to 600 nm, peaking notably at 400 nm. Furthermore, the TL intensity profile exhibited two distinct peaks at 150 and 240℃. In a related study, Alvarez [121] proposed a modified sol-gel synthesis route that excluded alcohol-based precursors. This method produced TL characteristics with slightly different main peaks and fading behavior. The reproducibility reported in Alvarez's study was approximately 3.5%, consistent with the value observed for HAP synthesized via the hydrolysis method. However, both Rivera-Montalvo and

Alvarez did not fully characterize additional TL performance parameters, such as annealing behavior, which is important for evaluating the material's suitability in practical dosimetric applications.

Electron paramagnetic resonance (EPR) is a technique used to detect unpaired electrons in irradiated materials and provides insight into radiation-induced defect structures [123]. In the study by Ziaie [120], HAp synthesized via the microwave-assisted method exhibited a stable and linear EPR response with increasing radiation dose. Previous research has shown that, in certain glass materials, EPR responses correlate with thermoluminescence (TL) behavior, particularly due to shared mechanisms involving radiation-induced trap states [124]. Based on this correlation, it can be tentatively hypothesized that HAp produced by the same method may also exhibit a linear TL response. However, this relationship is material-dependent and requires further experimental validation, as EPR–TL correlations are not universally applicable. Table 11 summarizes the TL characteristics and performance of HAp synthesized via different methods, including comparisons between undoped and doped forms.

Table 11. Experimental outputs of the dosimetric characteristics of HAp. The table is created by the author and the data is provided in the references available within the table.

Synthesis Methods	Main Peak (℃)	Emission Spectra (nm)	Fading (25℃)	Dose Range (Gy)	Reproducibility %	Heating Rate (℃/s)
Hydrolysis	200 [22]	N/A	Fast fading at low temperatures 32% after one month (RT) [22]	25-1000 (linear) [22]	±3.5% [22]	5
Hydrothermal [120]	-141.15	350-600	N/A	10^{-5}-0.87 (linear)	N/A	N/A
Sol-gel [21]	150 and 240	350-600, with a pronounced peak observed at 400	9% over 90 days	1-100 (linear)	N/A	10
Sol-gel [121]	200 and 300	N/A	15% over 90 days	25-100 (linear)	±3.5%	10
Microwave [120]	N/A	N/A	N/A	Linear and constant EPR response	N/A	N/A

Chapter IV. Advancement of Boron-doped Hydroxyapatite on Neutron Capture Therapy for Neutron Delivery Systems

4.1. Introduction

As a novel cancer treatment solution, Boron Neutron Capture Therapy (BNCT) offers a non-invasive and targeted radiotherapeutic approach that enables selective destruction of malignant cells while sparing healthy tissue. Its core principle lies in the targeted administration of boron-containing agents to tumor cells, followed by neutron irradiation, which induces the ^{10}B (n, α) ^{7}Li reaction. As shown in Figure 20, a detailed procedure of BNCT is provided. Particularly, the radionuclide boron-10 (^{10}B) is delivered intravenously via boron-containing compounds designed to preferentially accumulate in tumor tissues. Once sufficient uptake is achieved, patients are exposed to an external thermal neutron beam, typically generated by accelerator-based neutron sources. These thermal neutrons penetrate tissue and interact with the ^{10}B atoms localized within tumor cells, initiating the nuclear reaction $n + {}^{10}B \rightarrow {}^{11}B^* \rightarrow {}^{7}Li$ (0.84 MeV) + ^{4}He (1.47 MeV) + γ (0.478 MeV) [125, 126]. The energy values 0.84, 1.47, and 0.478 MeV correspond to charged particles, lithium, helium, and gamma photons, respectively. This reaction produces high-energy alpha particles and recoiling lithium nuclei, both of which exhibit high LET (linear energy transfer) characteristics and short penetration ranges (approximately 4–8 μm, roughly the diameter of a single cell). These characteristics allow for highly localized energy deposition, resulting in direct DNA double-strand breaks and effective tumor cell destruction [1, 2, 6, 127, 128]. The neutron capture cross-section of boron-10 (~3850 barns) is significantly larger than that of hydrogen (~0.332 barns) or nitrogen (~1.82 barns), both of which are prevalent in normal tissue. This difference enables thermal neutrons to selectively irradiate boron-enriched tumor regions while sparing surrounding healthy cells [5, 13].

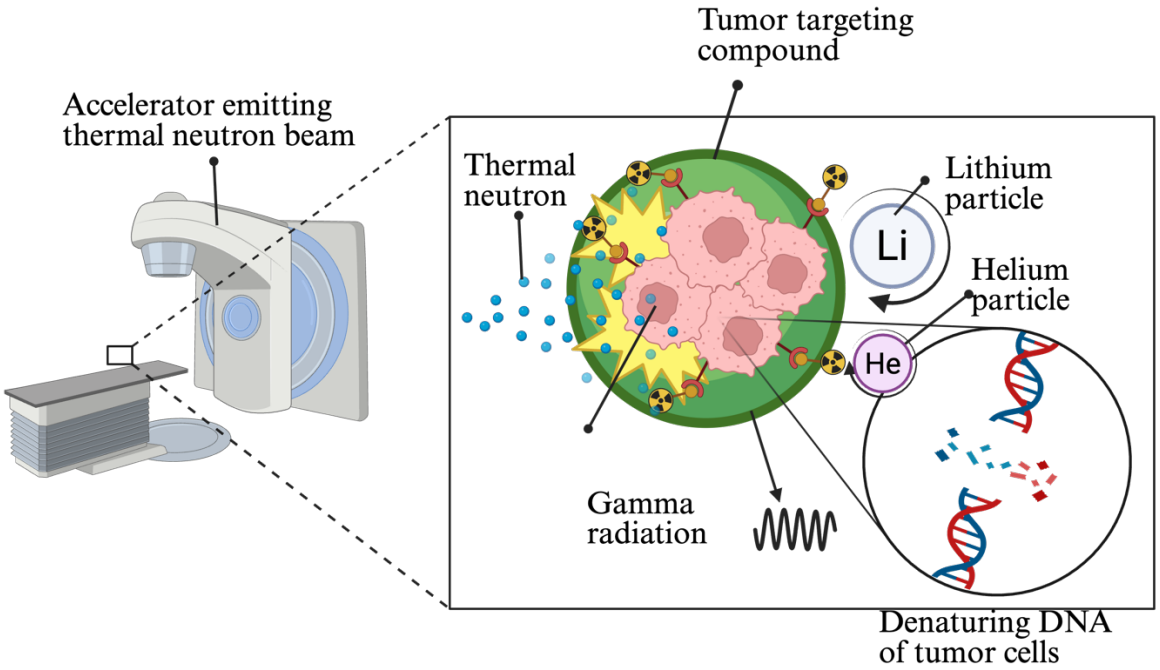

Figure 20. Schematic illustration of the boron neutron capture therapy (BNCT) procedure. The figure is created by the author based on the description from [126, 129].

In addition to its favorable physical characteristics, BNCT offers other promising advantages, including reduced systemic toxicity, localized treatment, and relatively lower overall cost, as it typically requires only two to three irradiation sessions [6]. Despite its conceptual appeal, early BNCT efforts were hindered by insufficient tumor selectivity and limited neutron penetration. A major breakthrough came in 1968, when Japanese researchers successfully employed BNCT using sodium borocaptate (BSH, $Na_2B_{12}H_{11}SH$) to treat malignant brain and neck tumors. BSH demonstrated the ability to localize in glioma tissue without crossing the blood-brain barrier [12, 125]. In recent years, BNCT has made significant clinical strides. In 2020, Japan became the first country to offer BNCT under national health insurance coverage and installed accelerator-based thermal neutron sources in hospitals across Japan, the United States, and China [1, 5]. Although BNCT has been clinically applied to various malignancies, the development of novel boron delivery systems, particularly nanoparticle-based carriers, remains an active area of research aimed

at enhancing treatment specificity, biocompatibility, and overall therapeutic efficacy [6]. Given its widespread biomedical applications and favorable physicochemical properties, HAp emerges as a promising candidate [31]. This thesis, therefore, focuses on a theoretical exploration of HAp's feasibility in boron-doped form as a multifunctional carrier in BNCT.

4.2. The Impacts of Neutron Beam Characteristics on BNCT Efficacy

Ensuring the neutron penetration depth and the boron concentration in tumors is paramount. To enhance therapeutic efficiency and diminish adverse side effects, several considerations should be taken on both the nature of neutrons as well as material properties. The nature of the incident neutrons, including their energy and fluence, is important. These parameters influence both the penetration depth and the therapeutic dosage delivered to the tumor tissue during irradiation, which can localize enough boron and induce a cytotoxic effect [3]. Higher energy enables neutrons to penetrate deeper into tumors. The limited penetration ability (~2 cm) allows thermal neutrons to treat surface tumors through intraoperative irradiation. Epithermal neutrons can penetrate tissues up to ~6 cm without surgical exposure. While fast neutrons offer deeper tissue penetration, they pose a higher risk of collateral damage due to their less selective energy deposition [3, 5, 13]. In contrast, this thesis focuses exclusively on thermal neutrons, as boron exhibits a significantly larger capture cross-section at thermal energies, making it more effective for targeted BNCT applications. Regarding the neutron fluence, a threshold of 10^{12} neutrons/cm² is generally required to initiate sufficient ^{10}B (n, α) ^{7}Li reactions, corresponding to a fluence rate of 10^{9} neutrons/cm²/s over one hour [3, 5, 13].

Meanwhile, boron carrier materials have to satisfy several requirements. First, they must exhibit low systemic toxicity [1, 6]. Second, they are required to deliver a therapeutic amount of boron to tumors, ranging from 20 to 35 μg/mL or approximately 10^{9} boron atoms per cell [5, 13].

According to clinical dosage guidelines in Japan, a 60 kg patient must receive 30 g of boron agents within 3 hours before neutron irradiation [5]. Moreover, these carriers must combine high solubility in aqueous environments with enhanced permeability and retention (EPR) effects for prolonged tumor retention times and rapid clearance from non-targeted tissues [1, 6, 13].

4.3. Conventional and Nanomaterial-Based Boron Agents

The earliest and most widely used boron-containing agents are sodium borocaptate (BSH, $Na_2B_{12}H_{11}SH$) and boronophenylalanine (BPA) [128, 130]. Specifically, BSH was first introduced in 1968 by Hatanaka for the treatment of malignant brain tumors due to its high solubility, strong boron-loading capacity, and ability to localize in glioma tissue beyond the blood-brain barrier [131]. Mishima introduced BPA to treat melanomas and cancers in 1987 [132]. However, BPA suffers from poor aqueous solubility and a limited boron payload, carrying only one boron atom per molecule [1]. Furthermore, pure BSH and BPA exhibit low tumor specificity, resulting in potential systemic toxicity and suboptimal tumor retention [6]. Therefore, it is necessary to innovate multifunctional materials to address these problems.

In recent years, materials scientists have explored diverse boron-containing carriers, ranging from low-molecular-weight compounds to high-molecular-weight polymers, liposomes, dendrimers, and nanoparticles to enhance tumor targeting and mitigate off-target toxicity [1, 6, 133]. In particular, nanomaterials have been widely investigated, including polymeric, lipid-based, and HAp nanoparticles. These nanomaterials offer several advantages, namely uniform and tunable pore sizes, nanoscale dimensions (10–20 nm), high surface-area-to-volume ratios, and improved EPR effects [20, 134]. These features enhance targeted delivery, prolong tumor retention, and improve drug release profiles.

4.4. Synthesis Methods for Boron-Doped Hydroxyapatite (BHA)

Beyond its therapeutic applications, boron incorporation into HAp enhances various material properties relevant to biomedical use. Changes in crystallinity and elemental composition can significantly influence performance metrics such as bioactivity, biocompatibility, and mechanical integrity [135, 136]. In materials science, porosity and other structural attributes are highly sensitive to both precursor selection and synthesis methods. Several established techniques have successfully produced boron-doped (BHA), yielding distinct morphological, compositional, and biological characteristics.

The most common boron precursors include boric acid and boron oxides, as these compounds dominate in nature and are chemically compatible with standard synthesis environments [28]. The final Ca:P:B ratio and related properties are strongly subject to the synthesis routes. For instance, Pazarçeviren reported that a Ca/P ratio of 1.6 optimized boron uptake [23]. However, this thesis adopts the stoichiometric ratio of Ca/(P+B) = 1.67, in accordance with the ideal formula for HAp ($Ca_{10}(PO_4)_6(OH)_2$) [150]. Table 12 summarizes the methods of synthesizing BHA.

4.5. Structural Characterization of Synthesized BHA

To analyze the changes in structures, compositions, and properties of BHA via various synthesis methods, previous studies implemented several characterization techniques such as X-ray diffraction (XRD), scanning electron microscopy (SEM), Fourier transform infrared spectroscopy, and Raman spectroscopy [26, 28, 137].

Table 12. Different synthesis routes of BHA together with pH, temperature, and other characteristics.

Synthesis Method	Precursors	pH	Temperature	Other Characteristics
Solid-state reaction	1. H_3BO_3, $CaCO_3$, and $(NH_4)_2HPO_4$ [138] 2. B_2O_3, $CaCO_3$, and $Ca_2P_2O_7$ [138]	-	1. Pelletization at 3 T/cm²; heat treatment at 1000°C in a platinum crucible 2. Calcination at 1200°C	The Ca/(P+B) ratio of 1.67 [28]
Microwave -assisted [23, 29, 139]	H_3BO_3, $Ca(NO_3)_2•4H_2O$, and $(NH_4)_2HPO_4$	10	900°C, 800 W of microwave power	Rapid reaction kinetics, fine particle control, and homogeneity
Sol-gel	1. H_3BO_3, $Ca(NO_3)_2•4H_2O$ and $(NH_4)_2HPO_4$ [140] 2. $(B(OC_3H_7)_3)$, $Ca(NO_3)_2•4H_2O$ and $(NH_4)_2HPO_4$ [141, 142]9/9/25 9:47:00 AM	>8	1) Stir while adding phosphate salt at 80°C for 2 h, and add ammonia water to adjust pH 2) Dry at 100°C for 12 h 3) Calcination from 800°C for 2 h	Obtain products with high surface area and bioactivity
Wet-chemical precipitation [28, 143]	Ca $(OH)_2$, Na_2HPO_4, and H_3BO_3	10.5	1 day	No requirement for heat, mechanical pressing, energy-efficient and scalable
Acid-base reaction [144, 145]	H_3BO_3, $Ca(NO_3)_2•4H_2O$ and $(NH_4)_2HPO_4$	10	Heat treatment at 60°C, then calcination at 110°C in the furnace	Chemical formula of $Ca_{10}(PO_4)_{5.8}(BO_4)_{0.2}(OH)_{1.6}$, indicating partial substitution of phosphate by borate ions

4.5.1. Crystallinity and Phase Identification of BHA

For synthesis routes involving high temperatures, typically above 850°C, the dehydration of HAp and the formation of trigonal BO_2 groups tend to significantly alter the BHA crystal structure, typically increasing the lattice parameter *c* and decreasing *a* [28]. In Table 13 and Figure 21, the XRD results of BHA based on current studies, including data on lattice parameters, unit cell volumes, and crystallinity, are summarized.

Table 13. X-ray diffraction results using the methods listed within the table.

Production method	Boron content (molar ratio)	Phase composition	Lattice parameter *a* (Å)	Lattice parameter *c* (Å)	Unit cell volume ($Å^3$)	Crystallinity (%)
Solid-state reaction [137]	0	HAp	9.418	6.884	528.8	-
	0.30		9.409	6.893	528.4	-
	0.50		9.399	6.890	527.9	-
Solid-state reaction [138]	0	HAp	9.406	6.882	527.3	-
	0.02		9.389	6.927	528.8	-
Microwave-assisted chemical precipitation [24]	0	HAp	9.422	6.881	529.1	95.19
	0.10		9.419	6.878	528.2	93.35
	0.50		9.415	6.885	528.6	89.90
Microwave-assisted [23]	0	HAp and TCP	9.422	6.888	611.5	86.34
	0.02		9.423	6.889	611.7	95.28
	0.10		9.404	6.908	611.0	98.68

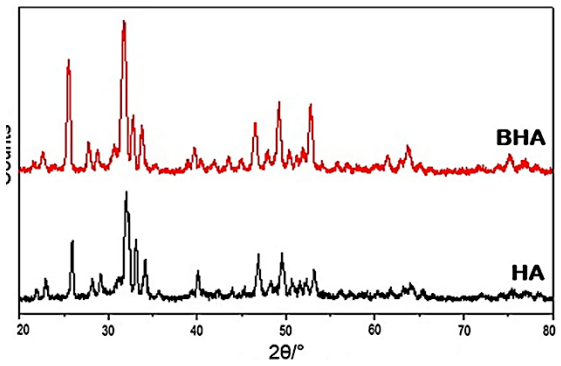

Figure 21. XRD results of products synthesized via the sol-gel method, taken from [142] with permission.

Figure 21 reveals the XRD results of BHA obtained via the microwave and sol-gel methods. Slight shifts in diffraction peaks were observed, but the characteristic reflections of HAp, namely (002), (211), (112), and (300), remain clearly identifiable in most samples [23, 142]. In general, an increase in boron content leads to a slight reduction in peak intensities and peak broadening. These changes suggest a decrease in crystallinity and a transition toward a more amorphous state upon boron incorporation. However, an exception was noted in Pazarçeviren's study, where increasing boron content correlated with increased crystallinity. This anomaly might be attributed to crystal growth within a biphasic system [23]. Regarding lattice parameters, XRD analysis confirms that the HAp structure remains hexagonal, typically indicated by equal or closely related values of *a* and *b* axes. With increasing boron incorporation, the *c*-axis tends to elongate, while the *a* and *b* lattice parameters contract. This structural distortion results in a net reduction of unit cell volume as the boron doping concentration increases [137, 138].

4.5.2. Morphology and Microstructure of BHA

In BHA, increasing the boron concentration generally results in finer grain sizes (see Table 14). This microstructural refinement leads to a larger specific surface area, which is beneficial for enhancing the material's bioactivity. These trends have been validated by Brunauer–Emmett–

Teller (BET) measurements, which confirm that higher boron incorporation correlates with increased surface area in BHA samples [23]. Based on SEM results in previous studies, BHA particles produced via most synthesis routes exhibit spherical shapes [23, 24, 138, 140, 143, 145]. Exceptions include samples obtained from the acid-base and solid-state reaction methods, which tend to yield less spherical and more irregular morphologies. Regarding particle agglomeration, the relatively uniform particle dispersion observed in BHA synthesized via wet precipitation may also contribute to improved packing density. While not a primary concern in BNCT, enhanced packing can support mechanical stability in multifunctional biomedical uses, such as bone-targeted therapies [143]. Table 14 summarizes the results related to particle sizes, porous sizes, and morphologies of synthesized BHA.

Table 14. Boron content, particles size, and morphology of BHA.

Production method	**Boron content (molar ratio)**	**Particle/grain size (nm)**
Solid-state reaction [138]	0	10^3-10^4
	0.02	
Microwave-assisted chemical precipitation [24]	0	106
	0.10	86
	0.50	85
Microwave-assisted [23]	0	-
	0.02	-
	0.10	-
Wet-precipitation method [143]	0.05	-
Sol-gel [140]	0.2	50
	0.5	20
Acid-base [145]	0.2	50-150

4.5.3. Water Retention of BHA

Water retention refers to the material's ability to retain water, which strongly influences its dissolution rate, ion release, and ultimately its bioactivity. The incorporation of boron into the HAp lattice has been shown to enhance water retention due to increased porosity of both HAp and BHA

structures [142]. The pores typically range from 100 to 400 µm in diameter, with 220 µm matching the average human bone diameter [28, 146]. This structural modification can also lead to variations in crystallinity depending on the synthesis conditions. For example, some studies report that boron doping leads to lower crystallinity in BHA synthesized via the wet and dry methods [28]. Reduced crystallinity increases the surface area, improving bioactivity and biodegradability, beneficial properties for drug delivery and selective degradation in acidic tumor microenvironments [20, 147].

4.5.4. Fourier-Transform Infrared (FTIR) Spectroscopy of BHA

Consistent findings across multiple studies confirm that borate groups (BO_3^{3-} and BO_2^-) are successfully incorporated into the HAp structure, replacing phosphate (PO_4^{3-}) and hydroxyl (OH^-) groups [23, 26, 29]. Table 15 summarizes the key vibrational peaks identified in FTIR spectra from several published studies.

Table 15. The characteristic peaks of BHA in FTIR studies [26, 29, 138, 145].

Synthesis route	Functional groups	Vibrational mode	Wavelength (cm^{-1})
Solid-state reaction [138]	PO_4^{3-}	v_4	569, 602
		v_3	961, 1050, 1092
	OH^-	v	3569, 3643
		liberational	631
	BO_3^{3-}	v_2	782-743
		v_3	1206-1312
	BO_2^-	v_3	2003
		linear	1933
Microwave-assisted wet chemical precipitation [24, 26, 29]	PO_4^{3-}	v_4	562-564, 598-600, 630
		v_3	1023-1024, 1087
		v_2	473-474
		v_1	962
	OH^-	v	3573
		liberational	628-630
	BO_3^{3-}	v_3	1217-1228, 1244
		v_2	744-783
	BO_2^-	v_3	1932, 2000
	B-type CO_3^{2-}	v	1365, 2343
Acid-base reaction [145]	PO_4^{3-}	v	966.5
	OH^-	v	564-630
	BO_3^{3-}	v	1086, 1368
Sol-gel [140]	PO_4^{3-}	v	561-602, 960-963
	OH^-	v	632-635, 3570
	BO_3^{3-}	v	782, 1208

4.5.5. Raman Spectroscopy of BHA

Raman spectroscopy offers valuable complementary insights, especially for distinguishing calcium phosphate (CaP) phases and identifying specific functional groups with higher spectral resolution. For instance, peaks at approximately 433 cm^{-1} and 962 cm^{-1} are characteristic of pure

HAp [140]. These peaks typically decrease in intensity with increasing boron concentration, indicating structural perturbations due to boron incorporation. Additionally, a Raman shift at ~1368 cm^{-1} has been attributed to borate groups, although the exact position may vary depending on the synthesis route and boron source used [137].

4.6 Biological and Therapeutic Potential of Boron-doped Hydroxyapatite (BHA)

To evaluate the biomedical applicability of synthesized BHA materials, both *in vitro* and *in vivo* experiments are essential. In the context of BNCT, key biological properties include biocompatibility, boron biodistribution, biodegradability, and tumor size control [135]. This section outlines the methods and outcomes used to assess the biological and therapeutic potential of BHA.

4.6.1. Biocompatibility and Bioactivity

Biocompatibility is a foundational requirement in any material used in the human body, as it ensures that the material and its degradation products are non-toxic and safe for human use [148]. This is typically assessed through cell culture assays, where materials are incubated with cells over a period of days, and cell viability is quantitatively measured [135]. In the case of BHA, biocompatibility is strongly influenced by the boron doping concentration. Numerous studies have demonstrated that boron incorporation enhances cell behavior and viability [26, 149]. For example, increased boron content correlates with improved cell viability, indicating the non-cytotoxic nature of BHA and its capacity to support cell proliferation. As shown in Figure 22, BHA synthesized via the microwave-assisted method at a boron doping concentration of 0.5 exhibited the highest cell viability over time [24]. However, while increased boron content generally improves biocompatibility, as previously mentioned, excessive boron concentrations can become cytotoxic, suggesting a therapeutic limit beyond which further doping may compromise cell health [25].

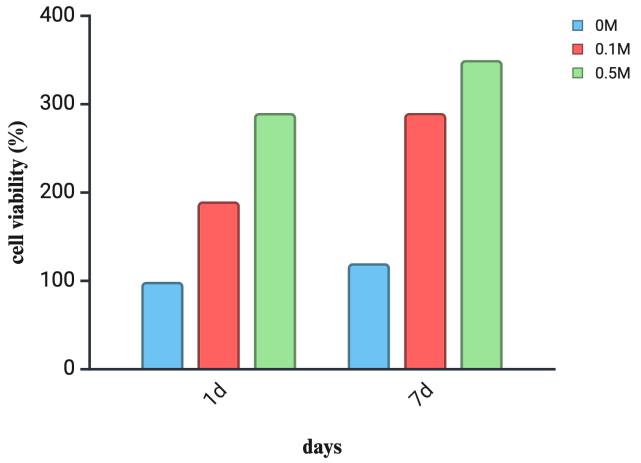

Figure 22. The biocompatibility study of BHA, incubated for 7 days [Jodati 2022].

Bioactivity, defined as the ability of a material to interact with biological tissues or physiological fluids, is a critical parameter in BNCT. It is typically influenced by factors such as material porosity and phase composition [146]. One common method to assess bioactivity involves analyzing BHA deposition and protein absorption in simulated body fluids [23], while the specific protein type used in the absorption test is not reported. The Pazarçeviren's study demonstrated that higher boron content enhances the performance in protein absorption of BHA. Other studies have also demonstrated that stoichiometric HAp shows the highest bioactivity, and that bioactivity increases with rising boron concentrations [23]. Furthermore, elevated ion release of calcium, phosphorus, and boron serves as a proxy for bioactivity in a human-simulated environment [29]. In the bioactivity test (see Figure 23), BHA is soaked in a Ca/P supersaturated solution. Excessive calcium or phosphorus ions will combine with negative ions of PO_4^{3-} on the BHA surface, inducing a decrease in calcium or phosphorus concentrations. In this incubation process, boron ions are released from the structure, increasing their concentration in the solution. In the boron ion release test, increased boron content may promote secondary interactions between boron and phosphate ions, resulting in additional release events [24].

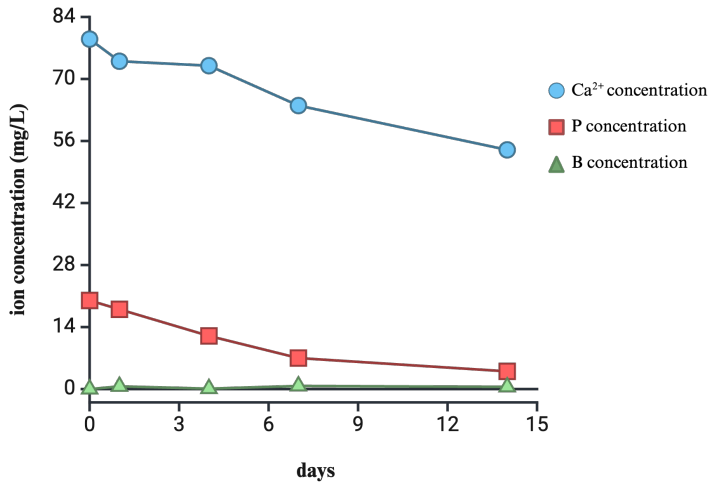

Figure 23. The bioactivity study of BHA, as reflected by the ion release study [Jodati 2022].

Although BNCT does not require boron to exist as free ions, the degradation behavior of BHA remains crucial for effective targeted delivery. Its degradation rate, which influences boron accumulation in tumor tissues, is affected by factors such as moisture content, particle size, and the internal porosity of BHA particles, referring to the volume and connectivity of pores that impact fluid permeability and dissolution [150]. Temperature is also a factor, but is typically assumed constant at physiological temperature (37°C). A rapid ion release may cause tumor necrosis due to the burst effect, which poses major risks by exposing the patient to a high local drug dose [151, 152]. Therefore, achieving a controlled degradation profile is critical to ensure treatment efficacy by influencing biodistribution, sufficient boron retention, and safety during the irradiation time [153]. Kang's study (see Figure 24) demonstrates that boron is released at a steady rate from BHA synthesized via the wet precipitation method, ranging from 0.01 to 1 microgram [143].

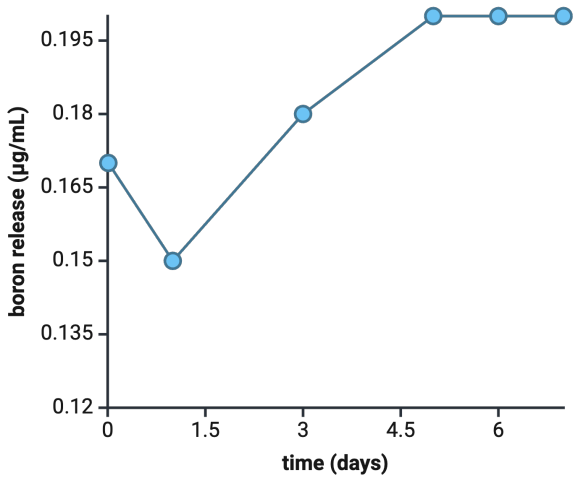

Figure 24. The boron release study [Gizer 2020].

4.6.2. Boron Biodistribution

Biodistribution, the process of tracking the locations and ways in which targeted compounds or drugs are distributed within an organism [154], is a critical parameter in BNCT, as it directly impacts the selectivity and efficacy of the therapy. Ensuring a high boron concentration in tumor tissues, while minimizing its presence in healthy tissues, is essential to achieve localized therapeutic effects and reduce side effects. In experimental studies, radiation treatment (RT) is commonly employed to evaluate boron concentration and its spatial distribution. This approach allows for the qualitative visualization of boron localization within biological tissues based on the ^{10}B (n, α) ^{7}Li neutron interaction. Typically, tissue samples are cryogenically treated using liquid nitrogen and then sectioned and placed onto a solid-state neutron detector. Darker staining in irradiated regions indicates a higher boron concentration and effective localization within tumor tissues [126].

As an alternative and complementary technique, particle spectroscopy provides a higher-resolution quantification of boron distribution. This method involves placing sliced tissue sections directly onto a silicon-based solid-state detector in a vacuum chamber under thermal neutron

irradiation, measuring the energy of emitted particles using a multichannel analyzer [126, 155]. Figure 25 illustrates the mechanism of determining boron distribution using both radiation treatment and particle spectroscopy.

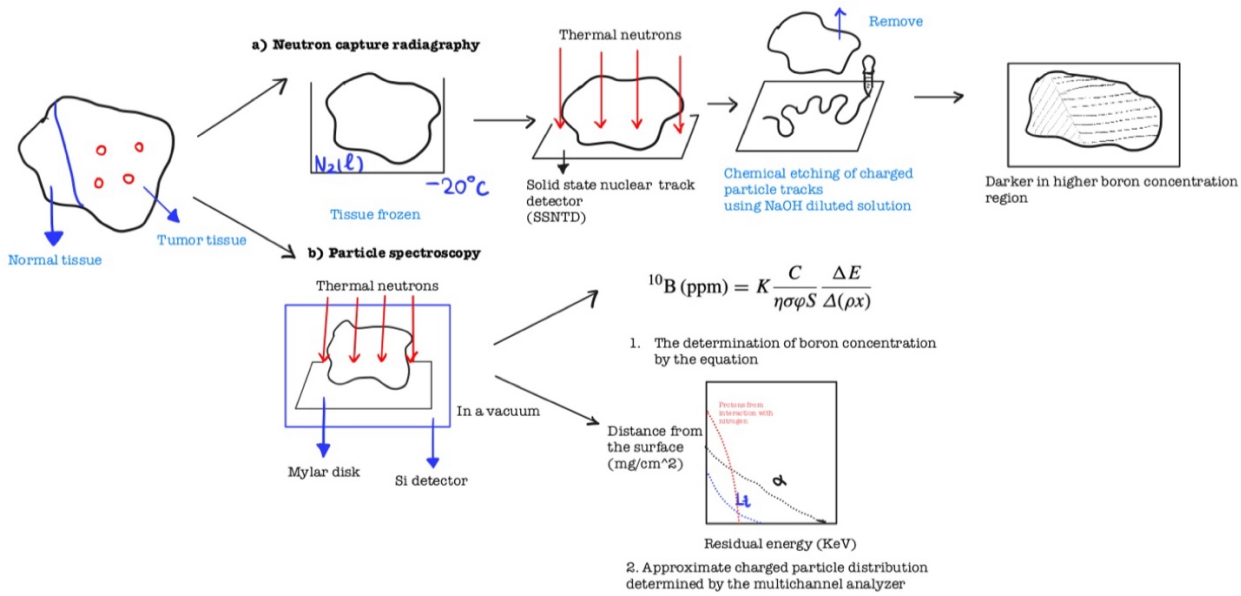

Figure 25. Working principles of a) radiation treatment; b) particle spectroscopy. The figure is created by the author based on the description from [126].

4.6.3. Relative Biological Effects (RBE) and Compound Biological Effects (CBE)

To ensure the success of BNCT, both the minimal tumor control dose and the maximum tolerable dose to healthy tissues must be carefully evaluated. As multiple components of irradiation contribute to biological effects, including high linear energy transfer (LET) particles and low LET gamma radiation, quantifying these effects requires more nuanced parameters. Therefore, researchers have introduced Relative Biological Effectiveness (RBE) and Compound Biological Effectiveness (CBE) to account for biological damage caused by different irradiation types. These metrics are essential for comparing the biological effectiveness of various radiation types at equivalent physical doses [128]. The RBE quantifies how effective a type of radiation (*e.g.*, X-rays or neutrons) is at causing biological damage compared to a reference, typically gamma

radiation [156]. To better estimate the therapeutic dose of high-LET (linear energy transfer) radiation beams in BNCT, the concept of the CBE was introduced by assuming that the boron compound is uniformly distributed in tissues at the same concentration as in blood [157]. The CBE is particularly valuable in clinical BNCT applications because both the boron concentration and neutron fluence in tissues can be measured or reasonably estimated during irradiation [157]. However, specific RBE and CBE values for BHA have not yet been defined previously [158].

In the equations used to define RBE and CBE, ED50 refers to the absorbed dose required to produce a 50% incidence of a specific biological effect. Meanwhile, thermal beams in this context typically represent protons generated from the $^{14}N(n,p)\ ^{14}C$ reaction and fast neutron recoil [157]:

$$RBE_{\ thermal\ beam} = (X\text{-ray } ED_{50} - \gamma\text{-ray dose}) / \text{thermal beam } ED_{50}$$

$$CBE = X\text{-ray } ED_{50} - (\text{thermal beam } ED_{50} \times RBE)/^{10}B\ (n, \alpha)^{7}Li\ ED_{50}$$

Measuring tumor size before and after treatment is a direct and effective method to assess the biological effects of BNCT. Upon thermal neutron irradiation, boron-loaded nanomaterials such as BHA produce alpha and lithium particles that selectively destroy tumor cells, resulting in a measurable reduction in tumor volume. Changes in tumor size can be quantitatively evaluated using radiographic imaging techniques. In addition to macroscopic tumor shrinkage, histological analysis provides insights into the cellular-level therapeutic effects. By examining tissue sections, researchers can determine the percentages of viable tumor nodules, necrotic areas, and fibrotic regions, indicators of successful therapy [135].

Chapter V. Discussion

To address current limitations, material innovation is under urgent investigation. Therefore, this chapter will discuss the research gaps that have been discovered in the previous studies, propose a theoretical material model with the performance predictions, and provide insights for future studies.

5.1. Gas Detectors: Toward Hybrid Architectures with Semiconductor Components

With the rapid advancement of semiconductor technologies, micropattern gas detectors have been replacing traditional gas-filled detectors for enhanced performance. These modern detectors utilize advanced fabrication techniques such as photolithography, laser machining, and selective etching, enabling finer electrode structures and improved performance. Four notable designs have emerged from this innovation, as illustrated in Figure 37 [32]:

1. **Microstrip Gas Chambers (MSGCs):** MSGCs resolve issues related to bulky insulating supports and provide faster charge collection. They are commonly used in particle tracking systems and photon detection setups such as CCDs [159].
2. **Gas Electron Multipliers (GEMs):** GEMs offer high gain in pure noble gases, along with excellent time and spatial resolution. Their ease of operation makes them suitable for high-energy physics, medical imaging, and astrophysics [160].
3. **Micromegas (MICRO-Mesh Gaseous Structures):** Based on planar electrode geometry, micromegas detectors provide high time and spatial resolution without degradation in detector or electronic performance. They are widely applied in particle physics and industrial sensing [161].

4. **Resistive Plate Chambers (RPCs):** RPCs are valued for their durability, cost-effectiveness, and fast signal response, making them useful in medical imaging and high-rate tracking environments [162].

Figure 26 summarizes various modern designs incorporated with semiconductor technologies, including microstrip gas chambers, gas electron multipliers, micromegas, and resistive plate chambers.

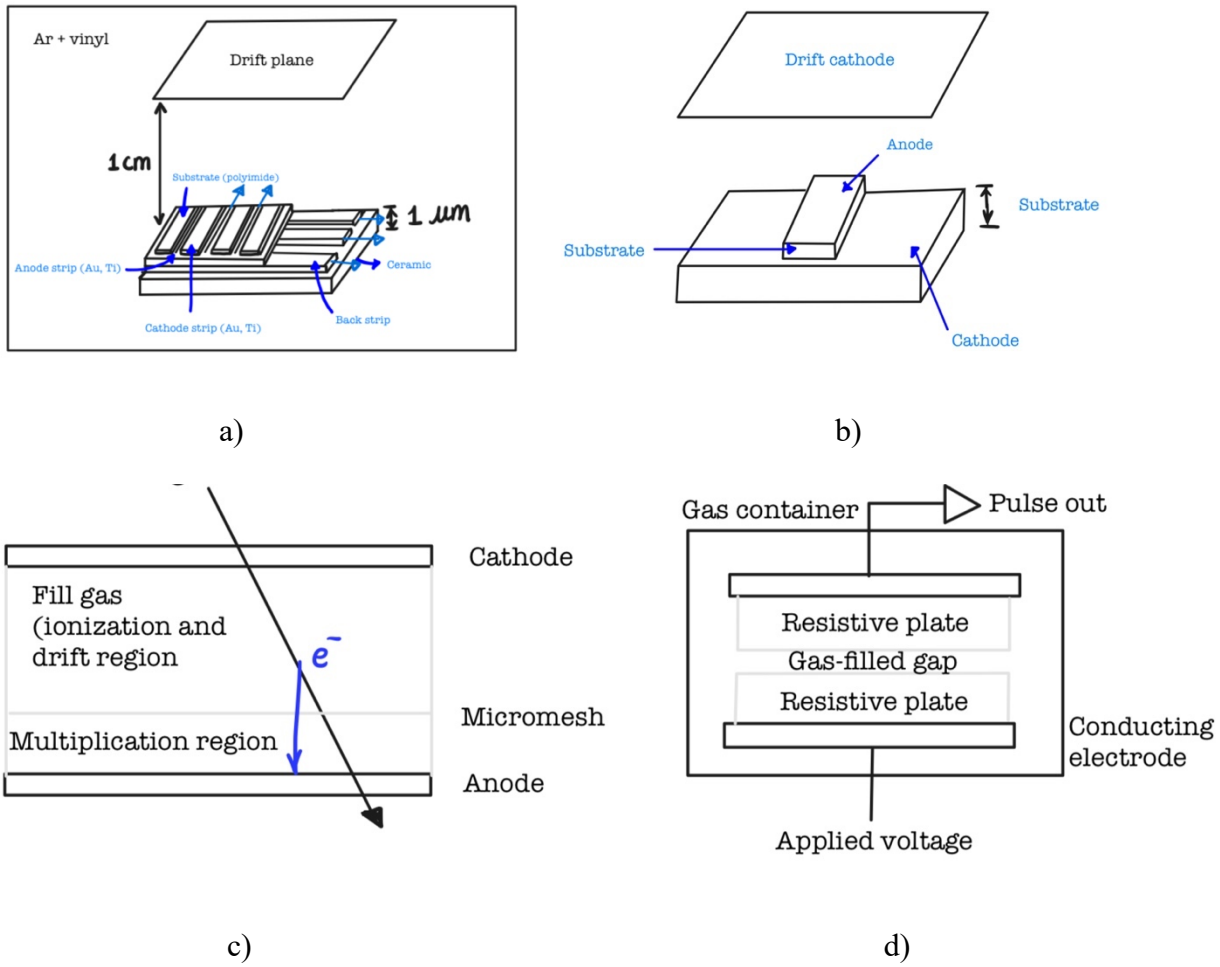

Figure 26. a) Microstrip gas chambers; b) gas electron multipliers; c) micromegas; d) resistive plate chambers. The figures are adapted from [32].

5.2. Scintillator Detectors

Based on current knowledge of neutron detection materials, an inconsistency in the reported bandgap energy value of gadolinium has been observed in Owens's study (previously cited in Table 6), as shown in Figure 27. The density value of the material discussed in Owens's study aligns with values reported in other literature, confirming that the germanium in question is in single-crystal form rather than a compound.

Table 2
Room-temperature properties of wide-band-gap compound semiconductor materials suitable for hard X- and γ-ray detectors. The abbreviations are: C = Czochralski, CVD = chemical vapor deposition, LEC = liquid encapsulated Czochralski, THM = traveler heater method, BM = Bridgman method, HPB = high-pressure Bridgman and VA = vertical ampoule method.

Material	Growth method	Atomic number	Density ($g\ cm^{-3}$)	Band gap (eV)	E_{pair} (eV)	Resistivity (Ω cm)	$\mu\tau$ (e) product ($cm^2\ V^{-1}$)	$\mu\tau$ (h) product ($cm^2\ V^{-1}$)
Ge	C	32	5.33	1.57	4.6	50	1	1

Figure 27. The semiconductor properties of elemental germanium. The figure is adapted from [94].

Owens reports a band gap value of 1.57 eV for the elemental germanium fabricated via the Czochralski method for use in planar detector systems [94]. This value significantly deviates, by nearly 60%, from the widely accepted band gap of approximately 0.66 eV, as reported by Lutz and Buchtela [93, 95]. While further standardized studies are needed to resolve this discrepancy, several factors could contribute to such variation. First, differences in crystal growth methods (*e.g.*, Czochralski vs melt-grown) may result in variations in crystallinity or introduce impurities. Second, synthesis conditions such as temperature, pressure, and doping concentration can alter the material's electronic band structure. Third, the discrepancy may arise from the nature of the band gap, whether the measurement reflects a direct or indirect transition. Finally, different measurement techniques (*e.g.*, optical absorption vs. electrical conductivity) can yield slightly different band gap values. However, while such factors may explain minor deviations, the

magnitude of the discrepancy suggests a potential reporting error or typographical oversight in Owens's study, particularly given that Owens also stated the typical bandgap energy range for elemental germanium to be 0.50–0.75 eV.

5.3. Dosimetry

Overall, HAp exhibits promising thermoluminescent (TL) properties across various synthesis methods, although specific performance metrics, such as fading, peak intensity, and dose response, may vary depending on the synthesis conditions. In terms of the thermoluminescent intensity profiles, both hydrothermal and hydrolysis methods produced single peaks, although the peak intensity for the hydrolysis method was relatively low. This suggests that these materials may contain traps of different depths, capable of releasing charge carriers at varying temperatures. The thermoluminescent (TL) response of HAp was consistently proportional to the absorbed dose across a wide range of absorbed dose values, validating its reliability for radiation dosimetry. Fading behavior, while slightly higher than that of conventional TL materials, was most stable in HAp synthesized via the sol-gel method using ethanol. The reproducibility results from hydrolysis-based HAp were comparable to those from sol-gel synthesis, indicating radiation resistance and the ability to generate consistent signal output.

However, other parameters (*e.g.*, relative sensitivity, annealing behaviors, and heating rate) are similarly important to evaluate the TL response of HAp. For instance, annealing behaviors can indicate the properties of reusing the materials by restoring the material properties while reversing radiation damage. Although HAp appears to have shown partial experimental validation on the most important TL properties (*e.g.*, dose response) in many studies, the absence of standardized criteria for fading and the limited data on sensitivity and annealing behavior highlight the need for further investigation before HAp can be confirmed as a viable TL dosimetric material.

5.4. Boron Neutron Capture Therapy (BNCT)

Clinical and experimental findings suggest that BHA exhibits excellent potential as a boron delivery material for BNCT. *In vitro* cell culture and calcium ion release studies confirm BHA's biocompatibility and bioactivity, with a boron doping concentration around 0.5 showing optimal results in terms of cell viability and minimal cytotoxicity. These properties make BHA a promising candidate for both bone tissue engineering and targeted tumor therapy. Furthermore, a Ca/P ratio of 1.67 has been associated with maximal bioactivity, as reflected in protein adsorption and ion release assays. Despite these strengths, several questions remain unresolved:

- Which synthesis method(s) is(are) the most effective one(s) to incorporate the therapeutic amount of boron atoms?
- What amounts of precursors need to be used to achieve nanoparticles with desired performance in BNCT?
- In the currently available studies, silicon-based solid-state detectors are used to test biodistribution. Can alternative detector technologies, such as solid-state neutron detectors, offer improved resolution or sensitivity in biodistribution assessments compared to conventional silicon-based systems?
- In this study, the in vitro dosimeter is used to conduct the total radiation doses within the whole body. Is there any *in vivo* dosimeter design that can measure internal radiation doses so that researchers can better control the irradiation doses to threshold levels?

5.5. Sensor Design for Boron Neutron Capture Therapy and Expected Dosimetric Response

Figure 28a-e demonstrates the proposed model for therapeutic process using BHA and HAp materials. In this concept, boron-doped hydroxyapatite (BHA) and pure hydroxyapatite (HAp)

are intravenously injected into surface-leveled tumor tissues (see Figure 28a). Due to boron's tumor selectivity, attributed to the alpha particle emission from the boron nuclear reaction [27], it is assumed that BHA is able to accumulate in the tumor cell region while HAp uniformly disperses throughout the normal tissue (see Figure 28b). Within a short period, boron atoms spread out as BHA diffuses in the tumor microenvironment. Upon thermal neutron beam irradiation, boron-neutron capture reactions are triggered, producing alpha particles and lithium nuclei that are detrimental to the tumor cells (see Figure 28c). After that, the damaged tumor cells are cleared by the immune system (see Figure 28d). In the meantime, HAp contributes by absorbing and storing additional radiation in the surrounding healthy tissue, thus reducing collateral damage. Since the tumor microenvironment typically does not reach the pH required for HAp degradation and HAp is part of human bone, HAp is expected to remain in place to support cell growth and tissue regeneration following tumor elimination. To monitor radiation dose during the therapy, an external luminescence dosimeter is attached via skin-mounted patches (see Figure 28e). Radiation is then transmitted through the conduit from the body to the luminescent dosimeter, where radiation is measured as electrical signals converted into luminescence spectra. This suggests that researchers are able to determine the efficient doses of neutron irradiation.

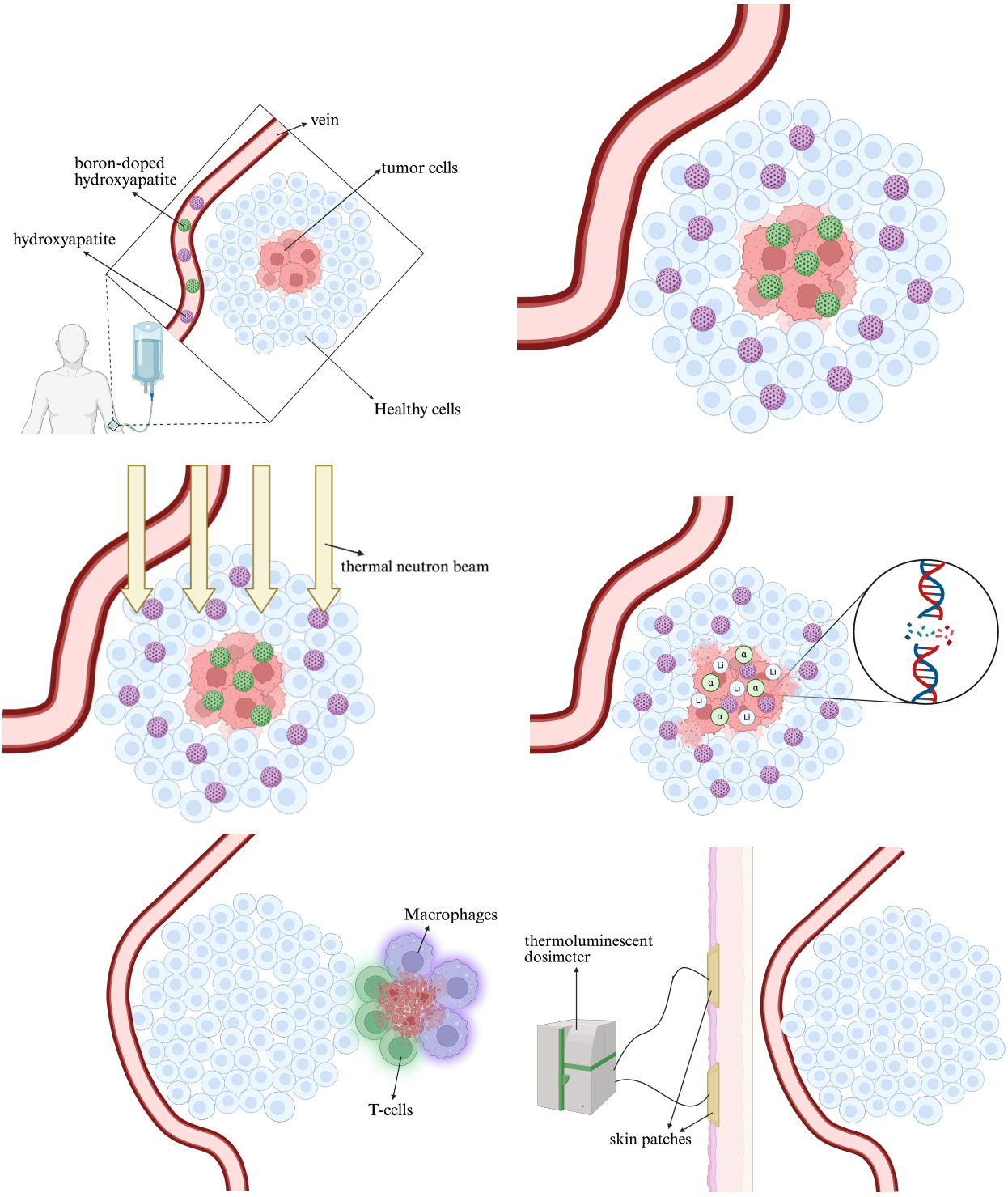

Figure 28. Conceptual model of tumor cell elimination via BHA and additional radiation absorption via HAp. During the therapeutic session, radiation doses are conducted to a luminescent dosimeter in vitro via the conductive tubes (see parts a-e).

To obtain BHA and HAp materials using safe, non-toxic precursors, and energy-efficient methodologies, the synthesis routes from Rivera-Montalvo [21] and AlHammad [140] studies are tailored. The precursors and conditions for synthesizing HAp and BHA are similar. Specifically, to prepare HAp nanoparticles, a P_2O_5-ethanol solution is added to a $Ca(NO_3)_2 \cdot 4H_2O$ solution and stirred for 1 h at room temperature. The resulting mixture is then heated to 56°C for 14 h before being cooled to room temperature, leading to precipitation of HAp. Next, for BHA nanoparticle synthesis, $(NH_4)HPO_4$ and H_3BO_3 are mixed with dissolved $Ca(NO_3)_2 \cdot 4H_2O$ and the pH is adjusted using ammonia water. The resulting product is dried at 100°C for 12 h and calcinated at 800°C for 2 h. Based on previous studies [23], HAp doped with 0.05 M boron exhibits optimal biological performance, with boron substituting exclusively for phosphate groups. Thus, the chemical formula for BHA proposed in this thesis is $Ca_{10}(PO_4)_{5.5}(BO_3)_{0.5}(OH)_2$. In order to achieve this amount, we need to prepare 400 to 700 mg/mL BHA in phosphorus buffer solution and incubate it.

Prior characterization studies further support that BHA is capable of improving the BNCT efficacy in tumor tissues. First, XRD results from Atila's study [142] show that decreased crystallinity increases surface area and improves BHA's bioactivity. This promotes better tissue integration and cell growth after tumor removal. Atila also reported that boron incorporation enhances water retention due to BHA's porous structures [142]. Higher water retention benefits the delivery system, improving the biodistribution of the material and reducing suboptimal tumor uptake. SEM analysis further confirms that the nanoscale size of BHA increases surface area, enabling drug delivery with higher precision [163]. In addition, the boron content enhances BHA's protein absorption capability, indicating better cellular compatibility and proliferation potential.

Given BHA's favorable biodistribution and high neutron cross-section to thermal neutrons, its relative biological effectiveness (RBE) and compound biological effectiveness (CBE), indicating the effectiveness for BNCT, this material is expected to be satisfactory. In terms of the effective doses, the neutron fluence typically used in BNCT is about 10^{12} neutrons/cm^2, equivalent to approximately 30 Gy, based on the conversion provided by Elmaghraby [164]. This value is below the reported dose limit for HAp [142], confirming that both HAp and BHA can absorb radiation effectively without compromising biocompatibility. Table 16 compares the BNCT properties of BHA to those of traditional materials.

Table 16. The BNCT property comparison between traditional materials and BHA.

	Traditional materials (BSH/BPA)	**BHA**
Side effects	Potential systemic toxicity and suboptimal tumor retention.	Safe to the human body.
TL performance	No applications on TL dosimetry.	Excellent TL properties for potential incorporation.

5.6. Future Directions

The incorporation of machine learning (ML) and artificial intelligence (AI) tools display great promise in prediction of materials chemistry. For example, ML models could predict both TL performance and therapeutic behaviors, such as tissue equivalence, boron delivery and release, as well as spatial distribution in tumors versus healthy tissue by modeling HAp and BHA with different particle sizes and boron concentrations. These advanced technologies can provide datasets to improve experimental design parameters, ultimately enabling personalized BNCT strategies, reducing cost-efficient material development time, and enhancing treatment efficacy and safety [163].

Conclusions

This thesis bridges neutron detection, dosimetry, and neutron capture therapy, proposing an innovative design for more precise and efficient cancer treatment. Through a comprehensive literature review, the parameters that play important roles in achieving this goal are evaluated. To begin with, neutron detectors, including gas-filled, scintillator, and semiconductor detectors, are described providing essential information about neutron characteristics, such as energy and fluence. These characteristics can later be read out using pulse-height spectra and applied to various applications. For instance, fast neutrons are more suitable for treating cancer in depth, whereas thermal neutrons are often used for surface tumors. In this thesis, thermal neutrons with energies ranging from 0.01 to 0.1 eV and a fluence of 10^{12} neutrons/cm^2 are of specific interest in the context of neutron capture therapy. Next, because neutron radiation is harmful but invisible to naked eyes, various dosimeters are described to quantify radiation doses. In particular, luminescence dosimeters operate by absorbing and converting radiation into electrical signals. Upon heated or light stimulation, these signals release luminescence that can be read to determine the absorbed dose. Lastly, neutron capture therapy refers to a therapeutic method based on neutron-nucleus interactions that produce charged particles capable of damaging tumor cells. This thesis focuses on boron neutron capture therapy (BNCT), leveraging the high thermal neutron absorption cross-section of boron-10 through the ^{10}B (n, α) ^{7}Li reaction. Boron also inherently exists in the human body and exhibits tumor selectivity, enhancing the efficacy of localized cancer treatment.

This thesis also studies material innovations to enhance dosimetric performance and targeted neutron delivery in BNCT. Hydroxyapatite (HAp) and boron-doped hydroxyapatite (BHA) are both shown to be promising candidates. Increased boron content enhances bioactivity and water retention, resulting in better distribution of BHA and HAp within tumors and normal cells.

This further promotes targeted and localized neutron therapy. HAp also demonstrates excellent thermoluminescence (TL) dosimetric properties, allowing it to store excess radiation over time, reducing the risk of damage to healthy tissues for localized radiation monitoring. Additionally, BHA's biocompatibility supports tissue regeneration for post-treatment and reduces side effects.

Built on the knowledge of these established fields, this thesis proposes a creative sensor design. After intravenous injection, HAp and BHA are expected to disperse across tumor and healthy tissues, respectively. Upon thermal neutron irradiation, boron undergoes nuclear reactions, releasing particles that destroy tumor cells while sparing healthy cells. After that, the immune system removes the damaged cells, while HAp remains to assist in radiation absorption and tissue regeneration. Meanwhile, an *in vitro* dosimeter is proposed to collect radiation doses through conductive tubes connected to skin patches, allowing for external dose monitoring. However, the heat requirement of TL dosimeters may limit *in vivo* applications.

While BHA shows promising characteristics as a dosimetric material and a boron nanovehicle, future studies remain necessary to address the research gaps in neutron detection, dosimetry, and cancer therapy. First, integrating semiconductor technology into conventional neutron detectors could enhance measurement accuracy. In addition, new synthesis methods should be explored to optimize boron loading while maintaining varying dosimetric and BNCT parameters. As previously mentioned, machine learning and artificial intelligence tools are useful in filling these research gaps. For example, designing effective nanomaterial synthesis routes and developing *in vivo* dosimeters for precise internal dose measurement further advancing BNCT's clinical viability. The integration of neutron detectors, dosimetry, and BNCT, enabled by the multifunctional properties of HAp and BHA, propels the development of cancer treatment, for selectively targeting tumors while minimizing harm to healthy tissues.

References (EndNote)

[1] Monti Hughes, A., & Hu, N. (2023). Optimizing boron neutron capture therapy (BNCT) to treat cancer: An updated review on the latest developments on boron compounds and strategies. Cancers, 15(16), 4091.

[2] Grupen, C., & Buvat, I. (Eds.). (2011). Handbook of particle detection and imaging. Springer Science & Business Media.

[3] Agosteo, S., Curzio, G., d'Errico, F., Nath, R., & Tinti, R. (2002). Characterisation of an accelerator-based neutron source for BNCT versus beam energy. Nuclear Instruments and Methods in Physics Research Section A: Accelerators, Spectrometers, Detectors and Associated Equipment, 476(1-2), 106-112.

[4] Wambersie, A., Barendsen, G. W., & Breteau, N. (1984). Overview and prospects of the application of fast neutrons in cancer therapy. J. Eur. Radiother.;(France), 5(3).

[5] Matsumoto, Y., Fukumitsu, N., Ishikawa, H., Nakai, K., & Sakurai, H. (2021). A critical review of radiation therapy: from particle beam therapy (proton, carbon, and BNCT) to beyond. Journal of personalized medicine, 11(8), 825.

[6] Ahmad, F. (2025). Boron Nanocomposites for Boron Neutron Capture Therapy and in Biomedicine: Evolvement and Challenges. Biomaterials Research, 29, 0145.

[7] Nesvizhevsky, V., & Villain, J. (2017). The discovery of the neutron and its consequences (1930–1940). Comptes Rendus. Physique, 18(9-10), 592-600.

[8] Diawara, Y. (Ed.). (2023). Neutron Detectors for Scattering Applications. Springer Nature.

[9] Parise, J. B. (2006). Introduction to neutron properties and applications. Reviews in Mineralogy and Geochemistry, 63(1), 1-25.

[10] Furrer, A., Mesot, J. F., & Strässle, T. (2009). Neutron scattering in condensed matter physics (Vol. 4). World Scientific Publishing Company.

[11] Chaturvedi, A., & Jain, V. (2019). Effect of ionizing radiation on human health. International journal of plant and environment, 5(03), 200-205.

[12] Goodhead, D. T. (2019). Neutrons are forever! Historical perspectives. International journal of radiation biology, 95(7), 957-984.

[13] Barth, R. F., Soloway, A. H., & Brugger, R. M. (1996). Boron neutron capture therapy of brain tumors: past history, current status, and future potential. Cancer investigation, 14(6), 534-550.

[14] Nahum, A. (2021). Principles and basic concepts in radiation dosimetry. In Handbook of Radiotherapy Physics (pp. Vol1-55). CRC Press.

[15] Locher, G. L. (1936). Neutron capture as a possible cancer therapy. Arner, Roentgenol. Radium Ther, 36, 1-5.

[16] Stewart, A. (1999). Detecting the health risks of radiation. Medicine, Conflict and Survival, 15(2), 138-148.

[17] Wahlstroem, B. (1994). Radiation in everyday life.

[18] Fiume, E., Magnaterra, G., Rahdar, A., Verné, E., & Baino, F. (2021). Hydroxyapatite for biomedical applications: A short overview. Ceramics, 4(4), 542-563.

[19] Ivanov, D. V., Shishkina, E. A., Osipov, D. I., Razumeev, R. A., & Pryakhin, E. A. (2015). Internal in vitro dosimetry for fish using hydroxyapatite-based EPR detectors. Radiation and environmental biophysics, 54(3), 257-263.

[20] Sun, W., Fan, J., Wang, S., Kang, Y., Du, J., & Peng, X. (2018). Biodegradable drug-loaded hydroxyapatite nanotherapeutic agent for targeted drug release in tumors. ACS applied materials & interfaces, 10(9), 7832-7840.

[21] Rivera-Montalvo, T., Romero, R. A., Hernandez, S. J. V., & Delgado, V. C. (2025). Synthesis and thermoluminescent characterization of synthetic hydroxyapatite as a detector for retrospective TL dosimetry. Applied Radiation and Isotopes, 220, 111790.

[22] Zarinfar, A., Shafaei, M., & Ziaie, F. (2015). Synthesis, characterization and thermoluminescence properties of nano-structure gadolinium doped hydroxyapatite (HAP: Gd). Procedia Materials Science, 11, 293-298.

[23] Pazarçeviren, A. E., Tezcaner, A., Keskin, D., Kolukısa, S. T., Sürdem, S., & Evis, Z. (2021). Boron-doped biphasic hydroxyapatite/β-tricalcium phosphate for bone tissue engineering. Biological Trace Element Research, 199(3), 968-980.

[24] Jodati, H., Tezcaner, A., Alshemary, A. Z., Şahin, V., & Evis, Z. (2022). Effects of the doping concentration of boron on physicochemical, mechanical, and biological properties of hydroxyapatite. Ceramics International, 48(16), 22743-22758.

[25] Abdelnour, S. A., Abd El-Hack, M. E., Swelum, A. A., Perillo, A., & Losacco, C. (2018). The vital roles of boron in animal health and production: A comprehensive review. Journal of Trace Elements in Medicine and Biology, 50, 296-304.

[26] Akbaba, S., Pazarçeviren, E., Karagüven, S. Ö. T., Evis, Z., & Tezcaner, A. (2025). Synthesis and characterization boron-doped hydroxyapatite for bone tissue engineering applications. Solid State Sciences, 107989.

[27] Kulkarni, S., Bhandary, D., Singh, Y., Monga, V., & Thareja, S. (2023). Boron in cancer therapeutics: An overview. Pharmacology & Therapeutics, 251, 108548.

[28] Uysal, İ., Yılmaz, B., & Evis, Z. (2020). Boron doped hydroxapatites in biomedical applications. Journal of Boron, 5(4), 199-208.

[29] Jodati, H., Evis, Z., Tezcaner, A., Alshemary, A. Z., & Motameni, A. (2023). 3D porous bioceramic based boron-doped hydroxyapatite/baghdadite composite scaffolds for bone tissue engineering. Journal of the Mechanical Behavior of Biomedical Materials, 140, 105722.

[30] Tannock, I. F., & Rotin, D. (1989). Acid pH in tumors and its potential for therapeutic exploitation. Cancer research, 49(16), 4373-4384.

[31] Lara-Ochoa, S., Ortega-Lara, W., & Guerrero-Beltrán, C. E. (2021). Hydroxyapatite nanoparticles in drug delivery: Physicochemistry and applications. Pharmaceutics, 13(10), 1642.

[32] Knoll, G. F. (2010). Radiation detection and measurement. John Wiley & Sons.

[33] Liu, J., Elsayed, A. M. M., & Medhat, M. E. (2022). Development of distributed and automated system for 14MeV neutron generator laboratory. Radiation Physics and Chemistry, 193, 109936.

[34] Hosseini-Ashrafi, M. E. (1990). The quantitative measurement of neutron induced activity in biomedical applications. University of Surrey (United Kingdom).

[35] Schmidt, K. H., & Jurado, B. (2018). Review on the progress in nuclear fission—experimental methods and theoretical descriptions. Reports on Progress in Physics, 81(10), 106301.

[36] Pietropaolo, A. (2023). The physical mechanisms of neutron detection. Contemporary Physics, 64(3), 194-223.

[37] Mijnheer, B. J. (1974). The angular dependence of fast neutron fission track registration. The International Journal of Applied Radiation and Isotopes, 25(8), 337-345.

[38] Milbrath, B. D., Peurrung, A. J., Bliss, M., & Weber, W. J. (2008). Radiation detector materials: An overview. Journal of Materials Research, 23(10), 2561-2581.

[39] An, B., Deng, Y., Jin, Z., & Sun, S. (2025). Scintillators for Neutron Detection and Imaging: Advances and Prospects. Advanced Functional Materials, 35(19), 2422522.

[40] Furrer, A. (1996). Cold neutron sources: prospects and applications. Physica Scripta, 1996(T66), 93.

[41] Rinaldi, R., Liang, L., & Schober, H. (2009). Neutron applications in earth, energy, and environmental sciences (pp. 1-14). Springer US.

[42] Hou, X., Wang, K., & Chai, C. (1996). Epithermal neutron activation analysis and its application in the miniature neutron source reactor. Journal of radioanalytical and nuclear chemistry, 210(1), 137-148.

[43] Gozani, T. (1994). Novel applications of fast neutron interrogation methods. Nuclear Instruments and Methods in Physics Research Section A: Accelerators, Spectrometers, Detectors and Associated Equipment, 353(1-3), 635-640.

[44] Gasnault, O., Feldman, W. C., Maurice, S., Genetay, I., d'Uston, C., Prettyman, T. H., & Moore, K. R. (2001). Composition from fast neutrons: Application to the Moon. Geophysical Research Letters, 28(19), 3797-3800.

[45] Peurrung, A. J. (2000). Recent developments in neutron detection. Nuclear Instruments and Methods in Physics Research Section A: Accelerators, Spectrometers, Detectors and Associated Equipment, 443(2-3), 400-415.

[46] Lakey, J. H. (2009). Neutrons for biologists: a beginner's guide, or why you should consider using neutrons. Journal of the Royal Society Interface, 6(suppl_5), S567-S573.

[47] Torres-Cortés, C. O., Perez-Arrieta, M. L., Vega-Carrillo, H. R., Garcia-Duran, A., & Vazquez-Bañuelos, J. (2025). Monte Carlo estimation of neutron absorbed dose in pure and rare earth-doped hydroxyapatite. Radiation Physics and Chemistry, 232, 112638.

[48] Crane, T. W., and M. P. Baker. 'Neutron detectors.' Passive Nondestructive Assay of Nuclear Materials 13 (1991): 1-28.

[49] Festa, G., Andreani, C., Arcidiacono, L., Grazzi, F., & Senesi, R. (2019). Neutron diffraction and (n, γ)-based techniques for cultural heritage. In Nanotechnologies and Nanomaterials for Diagnostic, Conservation and Restoration of Cultural Heritage (pp. 61-77). Elsevier.

[50] Sadykov, I. I., Zinov'ev, V. G., & Sadykova, Z. O. (2005). Neutron activation analysis of manganese mercury telluride. Journal of Analytical Chemistry, 60, 946-950.

[51] Kotlarchyk, M. (1999). Scattering theory.

[52] Talamo, A., & Gohar, Y. (2016). Neutron detector signal processing to calculate the effective neutron multiplication factor of subcritical assemblies (No. ANL-16/14). Argonne National Lab.(ANL), Argonne, IL (United States).

[53] Pakari, O., Lamirand, V., Perret, G., Braun, L., Frajtag, P., & Pautz, A. (2018). Current mode neutron noise measurements in the zero power reactor CROCUS. In EPJ Web of Conferences (Vol. 170, p. 04017). EDP Sciences.

[54] Pyeon, C. H., Chiba, G., Endo, T., & Watanabe, K. (2024). Neutron Measurements. In Reactor Laboratory Experiments at Kyoto University Critical Assembly (pp. 175-197). Singapore: Springer Nature Singapore.

[55] Carturan, S. M., Marchi, T., Fanchini, E., De Vita, R., Finocchiaro, P., & Pappalardo, A. (2014). Scintillator and solid-state neutron detectors and their applications. The European Physical Journal Plus, 129(10), 212.

[56] Sauli, F. (2015). Gaseous radiation detectors: fundamentals and applications (p. 497). Cambridge University Press.

[57] Pfeffermann, E. (2008). Proportional Counters. In The Universe in X-Rays (pp. 5-14). Berlin, Heidelberg: Springer Berlin Heidelberg.

[58] Kouzes, R. T., Ely, J. H., Erikson, L. E., Kernan, W. J., Lintereur, A. T., Siciliano, E. R., & Woodring, M. L. (2010). Neutron detection alternatives to 3He for national security applications. Nuclear Instruments and Methods in Physics Research Section A: Accelerators, Spectrometers, Detectors and Associated Equipment, 623(3), 1035-1045.

[59] Ravazzani, A., Para, A. F., Jaime, R., Looman, M., Ferrer, M. M., Peerani, P., & Schillebeeckx, P. (2006). Characterisation of 3He proportional counters. Radiation measurements, 41(5), 582-593.

[60] Desai, S. S., & Rao, M. N. (2021). Effect of temperature on performance of Boron Trifluoride (BF3) gas-based neutron proportional counters. Radiation Measurements, 144, 106593.

[61] Guo, E., Chen, J., Xiong, J., He, Z., Wang, C., An, H., & Dong, J. (2019). A neutron-diagnostic method using a BF3 detector array for ultrashort-pulse-laser neutron sources in strong gamma-ray environments. Journal of Instrumentation, 14(10), P10016.

[62] Lintereur, A., Conlin, K., Ely, J., Erikson, L., Kouzes, R., Siciliano, E., & Woodring, M. (2011). 3He and BF3 neutron detector pressure effect and model comparison. Nuclear Instruments and Methods in Physics Research Section A: Accelerators, Spectrometers, Detectors and Associated Equipment, 652(1), 347-350.

[63] Mehendale, S., Kanaki, K., Povoli, M., Samnøy, A. T., Tambave, G., Kok, A., & Hall-Wilton, R. (2020). Characterization of boron-coated silicon sensors for thermal neutron detection. Nuclear Instruments and Methods in Physics Research Section A: Accelerators, Spectrometers, Detectors and Associated Equipment, 972, 164124.

[64] Deng, C., Wang, Q., Wu, Y., Peng, S., Liu, F., Li, H., & Tuo, X. (2021). Preparation and characterization of boron films used for boron-lined gaseous neutron detectors. Journal of the Korean Physical Society, 79, 606-612.

[65] Aldhafeeri, T., Tran, M. K., Vrolyk, R., Pope, M., & Fowler, M. (2020). A review of methane gas detection sensors: Recent developments and future perspectives. Inventions, 5(3), 28.

[66] Bhike, M., Fallin, B., & Tornow, W. (2014). Measurements of the 40Ar (n, γ) 41Ar radiative-capture cross section between 0.4 and 14.8 MeV. Physics Letters B, 736, 361-364.

[67] Ni, K., Hasty, R., Wongjirad, T. M., Kastens, L., Manzur, A., & McKinsey, D. N. (2007). Preparation of neutron-activated xenon for liquid xenon detector calibration. Nuclear Instruments and Methods in Physics Research Section A: Accelerators, Spectrometers, Detectors and Associated Equipment, 582(2), 569-574.

[68] Mazed, D., Mameri, S., & Ciolini, R. (2012). Design parameters and technology optimization of 3He-filled proportional counters for thermal neutron detection and spectrometry applications. Radiation Measurements, 47(8), 577-587.

[69] Trenn, T. J. (1986). The Geiger-Müller Counter of 1928. Annals of Science, 43(2), 111-135.

[70] Remon, N. M., Hassan, C. M. T., Hassan, M. S., & Zakir, M. G. (2024). Build very simple design and cost effective Geiger-Muller counter. Journal of Recent Advances in Applied Sciences (pISSN 0970-1990), 39(01).

[71] Ghuge, N. N., Jasrotia, S., & Anamika, C. S. (2015). Geiger Muller: A thin end window tube radiation detector. International Journal of Research in Engineering and Technology, 4(5), 190-196.

[72] Zaidi, M. K., & Naeem, S. F. (2009). Gas-Filled and Plastic Scintillation Detectors: Advantages and Disadvantages. In New Techniques for the Detection of Nuclear and Radioactive Agents (pp. 181-192). Springer Netherlands.

[73] García-León, M. (2022). Scintillation Detectors. In Detecting Environmental Radioactivity (pp. 299-337). Cham: Springer International Publishing.

[74] Nakhostin, M. (2017). Signal processing for radiation detectors. John Wiley & Sons.

[75] Delage, M. È., & Beaulieu, L. (2018). Scintillation of organic materials. In Scintillation Dosimetry (pp. 3-20). CRC Press.

[76] Blasse, G. (1994). Scintillator materials. Chemistry of Materials, 6(9), 1465-1475.

[77] Gektin, A., & Korzhik, M. (2017). Inorganic scintillators for detector systems (pp. 20-77). Berlin, Germany:: Springer.

[78] Davidson, J. B. (1974). Fly's eye: a counting camera for thermal neutrons. Applied Crystallography, 7(3), 356-366.

[79] Ranucci, G., Goretti, A., & Lombardi, P. (1998). Pulse-shape discrimination of liquid scintillators. Nuclear Instruments and Methods in Physics Research Section A: Accelerators, Spectrometers, Detectors and Associated Equipment, 412(2-3), 374-386.

[80] Tyagi, M., Rawat, S., Kumar, G. A., & Gadkari, S. C. (2020). A novel versatile phoswich detector consisting of single crystal scintillators. Nuclear Instruments and Methods in Physics Research Section A: Accelerators, Spectrometers, Detectors and Associated Equipment, 951, 162982.

[81] Koshimizu, M. (2022). Recent progress of organic scintillators. Japanese Journal of Applied Physics, 62(1), 010503.

[82] Birks, J. B. (2013). The theory and practice of scintillation counting: International series of monographs in electronics and instrumentation (Vol. 27). Elsevier.

[83] Sangster, R. C., & Irvine Jr, J. W. (1956). Study of organic scintillators. The Journal of Chemical Physics, 24(4), 670-715.

[84] Cieślak, M. J., Gamage, K. A., & Glover, R. (2019). Critical review of scintillating crystals for neutron detection. Crystals, 9(9), 480.

[85] Schoppmann, S. (2022). Review of novel approaches to organic liquid scintillators in neutrino physics. Symmetry, 15(1), 11.

[86] Khan, S., Kim, H. J., Park, H., Ruqia, B., Lee, J. Y., Fawad, U., & Kang, S. J. (2015). Search for a new Li-based scintillator for neutron detection. Journal of the Korean Physical Society, 67, 1463-1468.

[87] Schardt, A. W., & Bernstein, W. (1953). Lithium Iodide Neutron Detector (Vol. 1156). United States Atomic Energy Commission, Technical Information Service.

[88] Reilly, T. D., Martin, E. R., Parker, J. L., Speir, L. G., & Walton, R. B. (1974). A continuous in-line monitor for UF6 enrichment. Nuclear Technology, 23(3), 318-327.

[89] Van Loef, E. V. D., Dorenbos, P., Van Eijk, C. W. E., Krämer, K., & Güdel, H. U. (2001). High-energy-resolution scintillator: Ce 3+ activated LaBr 3. Applied physics letters, 79(10), 1573-1575.

[90] Favalli, A., Wiggins, B. W., Iliev, M., Richards, C. G., Ogren, K., McLean, T. D., & Hehlen, M. P. (2025). Next-generation neutron detection using a 6Li glass scintillator composite. Communications Physics, 8(1), 10.

[91] Weber, M. J. (2002). Inorganic scintillators: today and tomorrow. Journal of Luminescence, 100(1-4), 35-45.

[92] van Eijk, C. W. (2004). Inorganic scintillators for thermal neutron detection. Radiation Measurements, 38(4-6), 337-342.

[93] Lutz, G. (2007). Semiconductor radiation detectors.

[94] Owens, A. (2006). Semiconductor materials and radiation detection. Synchrotron Radiation, 13(2), 143-150.

[95] Buchtela, K. (2005). Radiochemical methods| gamma-ray spectrometry.

[96] Zhang, Z., & Aspinall, M. D. (2021). Comparison of neutron detection performance of four thin-film semiconductor neutron detectors based on geant4. Sensors, 21(23), 7930.

[97] Gerrish, V. M. (1995). Characterization and quantification of detector performance. In Semiconductors and Semimetals (Vol. 43, pp. 493-530). Elsevier.

[98] Nolas, G. S., & Goldsmid, H. J. (2004). Thermal conductivity of semiconductors. In Thermal Conductivity: Theory, Properties, and Applications (pp. 105-121). Boston, MA: Springer US.

[99] Brooks, F. D. (1997, February). Neutron detectors and spectrometers. In International Conference Neutrons in Research and Industry (Vol. 2867, pp. 538-549). SPIE.

[100] McGregor, D. S., & Kammeraad, J. E. (1995). Gallium arsenide radiation detectors and spectrometers. In Semiconductors and Semimetals (Vol. 43, pp. 383-442). Elsevier.

[101] Straume, T. (1985). A radiobiological basis for setting neutron radiation safety standards. Health physics, 49(5), 883-896.

[102] Adlienė, D., & Adlytė, R. (2017). Dosimetry principles, dose measurements and radiation protection. Applications of ionizing radiation in materials processing. Vol. 1, 55-80.

[103] Nelson, F. R. T., Blauvelt, C. T. (2014). A Manual of Orthopaedic Terminology. United States: Elsevier/Saunders.

[104] Kron, T. (1999). Applications of thermoluminescence dosimetry in medicine. Radiation protection dosimetry, 85(1-4), 333-340.

[105] Liu, Y., Ma, L., Guo, J., Dong, G., Cong, J., Ji, Y., & Wu, K. (2018). Study of new practical ESR dosimeter based on carbonated hydroxyapatite and its dosimetric properties. Plos one, 13(5), e0197953.

[106] Izewska, J. O. A. N. N. A., & Rajan, G. (2005). Radiation dosimeters. Radiation oncology physics: a handbook for teachers and students, 36, 71-99.

[107] ML, A., Chatterjee, I., & Patil, P. (2015). Dosimetry in dentistry. Indian Journal of Dental Research, 26(2).

[108] Nanto, H., & Okada, G. (2022). Optically stimulated luminescence dosimeters: principles, phosphors and applications. Japanese Journal of Applied Physics, 62(1), 010505.

[109] Pradhan, A. S. (1981). Thermoluminescence dosimetry and its applications. Radiation Protection Dosimetry, 1(3), 153-167.

[110] Bos, A. J. J. (2001). High sensitivity thermoluminescence dosimetry. Nuclear Instruments and Methods in Physics Research Section B: Beam Interactions with Materials and Atoms, 184(1-2), 3-28.

[111] Nikaido, F., Abe, Y., Minami, T., Kuramoto, K., Yasui, T., Sakai, K., & Kuramitsu, Y. (2024). 3D track extraction from a fluorescent nuclear track detector via machine learning and an application to diagnostics of laser-driven ions. Review of Scientific Instruments, 95(10).

[112] Kortov, V. (2007). Materials for thermoluminescent dosimetry: Current status and future trends. Radiation Measurements, 42(4-5), 576-581.

[113] Yukihara, E. G., & McKeever, S. W. S. (2008). Optically stimulated luminescence (OSL) dosimetry in medicine. Physics in Medicine & Biology, 53(20), R351.

[114] Podgoršak, E. B. (2006). Radiation physics for medical physicists. Berlin, Heidelberg: Springer Berlin Heidelberg.

[115] Horowitz, Y. S., & Press, C. R. C. (Eds.). (1984). Thermoluminescence and thermoluminescent dosimetry (Vol. 1). Boca Raton: CRC Press.

[116] Bahl, S., Lochab, S. P., & Kumar, P. (2016). CaSO4: Dy, Mn: A new and highly sensitive thermoluminescence phosphor for versatile dosimetry. Radiation Physics and Chemistry, 119, 136-141.

[117] Kato, T., Kawano, N., Okada, G., Kawaguchi, N., & Yanagida, T. (2017). Comparative study of dosimeter properties between Al2O3 transparent ceramic and single crystal. Radiation Measurements, 107, 43-47.

[118] de Alencar, M. A. V. (2009). The TL and OSL study of hydroxyapatites for dosimetric applications.

[119] Lapraz, D., Baumer, A., & Iacconi, P. (1979). On the thermoluminescent properties of hydroxyapatite Ca5 (PO4) 3OH. physica status solidi (a), 54(2), 605-613.

[120] Ziaie, F., Hajiloo, N., Alipour, A., Amraei, R., & Mehtieva, S. I. (2011). Retrospective dosimetry using synthesized nano-structure hydroxyapatite. Radiation protection dosimetry, 145(4), 377-384.

[121] Alvarez, R., Rivera, T., Guzman, J., Piña-Barba, M. C., & Azorin, J. (2014). Thermoluminescent characteristics of synthetic hydroxyapatite (SHAp). Applied Radiation and Isotopes, 83, 192-195.

[122] Shafaei, M., Ziaie, F., Sardari, D., & Larijani, M. M. (2016). Thermoluminescence properties of gamma-irradiated nano-structure hydroxyapatite. Luminescence, 31(1), 223-228.

[123] Misra, M. G., & Kripal, R. (2012). EPR, optical absorption and superposition model studies of Fe3+-doped cesium chloride single crystals: a case of substitutional as well as interstitial sites. Molecular Physics, 110(24), 3001-3013.

[124] McKeever, S. W. S., Sholom, S., & Chandler, J. R. (2019). A comparative study of EPR and TL signals in Gorilla® glass. Radiation Protection Dosimetry, 186(1), 65-69.

[125] Lee, G. H., & Kim, J. T. (2014). Ultrasmall lanthanide oxide nanoparticles for biomedical imaging and therapy. Woodhead Publishing.

[126] Wittig, A., Michel, J., Moss, R. L., Stecher-Rasmussen, F., Arlinghaus, H. F., Bendel, P., & Sauerwein, W. A. (2008). Boron analysis and boron imaging in biological materials for boron neutron capture therapy (BNCT). Critical reviews in oncology/hematology, 68(1), 66-90.

[127] Zonta, A., Roveda, L., & Altieri, S. (2012). Liver metastases. In Neutron Capture Therapy: Principles and Applications (pp. 461-503). Berlin, Heidelberg: Springer Berlin Heidelberg.

[128] Fukuda, H. (2021). Response of normal tissues to boron neutron capture therapy (BNCT) with 10B-borocaptate sodium (BSH) and 10B-paraboronophenylalanine (BPA). Cells, 10(11), 2883.

[129] Sauerwein, W., Wittig, A., Moss, R., Nakagawa, Y., & Ono, K. (Eds.). (2012). Neutron capture therapy: principles and applications (pp. 1-12). Berlin, Heidelberg: Springer Berlin Heidelberg.

[130] Sweet, W.H. Early history of development of boron neutron capture therapy of tumors. J. Neurooncol. 1997, 33, 19–26.

[131] Hatanaka, H.; Nakagawa, Y. Clinical results of long-surviving brain tumor patients who underwent boron neutron capture therapy. Int. J. Radiat. Oncol. Biol. Phys. 1994, 28, 1061–1066.

[132] Suzuki, M.; Kato, I.; Aihara, T.; Hiratsuka, J.; Yoshimura, K.; Niimi, M.; Kimura, Y.; Ariyoshi, Y.; Haginomori, S.-I.; Sakurai, Y. Boron neutron capture therapy outcomes for advanced or recurrent head and neck cancer. J. Radiat. Res. 2014, 55, 146.

[133] Yanagië, H., Ogata, A., Sugiyama, H., Eriguchi, M., Takamoto, S., & Takahashi, H. (2008). Application of drug delivery system to boron neutron capture therapy for cancer. Expert opinion on drug delivery, 5(4), 427-443.

[134] Afzal, O., Altamimi, A. S., Nadeem, M. S., Alzarea, S. I., Almalki, W. H., Tariq, A., & Kazmi, I. (2022). Nanoparticles in drug delivery: from history to therapeutic applications. Nanomaterials, 12(24), 4494.

[135] Hsu, C. F., Liu, H. M., Peir, J. J., Liao, J. W., Chen, K. S., Chen, Y. W., & Chou, F. I. (2023). Therapeutic efficacy and radiobiological effects of boric-acid-mediated BNCT in an osteosarcoma-bearing SD rat model. Life, 13(2), 514.

[136] Callens, F., Vanhaelewyn, G., Matthys, P., & Boesman, E. (1998). EPR of carbonate derived radicals: applications in dosimetry, dating and detection of irradiated food. Applied magnetic resonance, 14(2), 235-254.

[137] Ternane, R., Cohen-Adad, M. T., Panczer, G., Goutaudier, C., Kbir-Ariguib, N., Trabelsi-Ayedi, M., & Massiot, D. (2002). Introduction of boron in hydroxyapatite: synthesis and structural characterization. Journal of Alloys and Compounds, 333(1-2), 62-71.

[138] Barheine, S., Hayakawa, S., Jäger, C., Shirosaki, Y., & Osaka, A. (2011). Effect of disordered structure of boron-containing calcium phosphates on their in vitro biodegradability. Journal of the American ceramic society, 94(8), 2656-2662.

[139] Aydın, N., Karaoğlanoğlu, S., Süloğlu, A. K., İdil, N., Demir, M., & Karakaş, İ. H. (2024). Investigation of cytotoxicity and antibacterial effect of boron-containing nano-hydroxyapatite. Journal of Stomatology, 77(2), 93-99.

[140] AlHammad, M. S. (2016). Nanostructure hydroxyapatite based ceramics by sol gel method. Journal of Alloys and Compounds, 661, 251-256.

[141] Piatti, E., Verné, E., & Miola, M. (2022). Synthesis and characterization of sol-gel bioactive glass nanoparticles doped with boron and copper. Ceramics International, 48(10), 13706-13718.

[142] Atila, D., Karataş, A., Evcin, A., Keskin, D., & Tezcaner, A. (2019). Bacterial cellulose-reinforced boron-doped hydroxyapatite/gelatin scaffolds for bone tissue engineering. Cellulose, 26(18), 9765-9785.

[143] Kang, Q., Wang, W., Wu, S., & Hu, G. (2025). B-doped nano-hydroxyapatite facilitates proliferation and differentiation of osteoblasts. Journal of Orthopaedic Surgery and Research, 20(1), 62.

[144] Çiftci, E., Köse, S., Korkusuz, P., Timuçin, M., & Korkusuz, F. (2015). Boron containing nano hydroxyapatites (Bn-HAp) stimulate mesenchymal stem cell adhesion, proliferation and differentiation. Key Engineering Materials, 631, 373-378.

[145] Ciftci Dede, E., Korkusuz, P., Bilgiç, E., Çetinkaya, M. A., & Korkusuz, F. (2022). Boron nano-hydroxyapatite composite increases the bone regeneration of ovariectomized rabbit femurs. Biological trace element research, 200(1), 183-196.

[146] Canillas, M., Pena, P., de Aza, A. H., & Rodríguez, M. A. (2017). Calcium phosphates for biomedical applications. Boletín de la Sociedad Española de Cerámica Y vidrio, 56(3), 91-112.

[147] Izumikawa, S., Yoshioka, S., Aso, Y., & Takeda, Y. (1991). Preparation of poly (l-lactide) microspheres of different crystalline morphology and effect of crystalline morphology on drug release rate. Journal of controlled release, 15(2), 133-140.

[148] Ramakrishna, S., & Huang, Z. M. (2016). Biocomposites.

[149] Ammar, M., Ashraf, S., & Baltrusaitis, J. (2023). Nutrient-Doped hydroxyapatite: Structure, synthesis and properties. Ceramics, 6(3), 1799-1825.

[150] Agostini, F., Sundberg, C., & Navia, R. (2012). Is biodegradable waste a porous environment? A review. Waste management & research, 30(10), 1001-1015.

[151] Pazarçeviren, A. E., Akbaba, S., Evis, Z., & Tezcaner, A. (2022). Versatile-in-all-trades: multifunctional boron-doped calcium-deficient hydroxyapatite directs immunomodulation and regeneration. ACS Biomaterials Science & Engineering, 8(7), 3038-3053.

[152] Brazel, C. S., & Huang, X. (2004). The cost of optimal drug delivery: reducing and preventing the burst effect in matrix systems.

[153] Zamani, F., Jahanmard, F., Ghasemkhah, F., Amjad-Iranagh, S., Bagherzadeh, R., Amani-Tehran, M., & Latifi, M. (2017). Nanofibrous and nanoparticle materials as drug-delivery systems. In Nanostructures for Drug Delivery (pp. 239-270). Elsevier.

[154] Singh, A. K. (2016). Principles of nanotoxicology. Engineered Nanoparticles, 171-227.

[155] Spurný, F., & Turek, K. (1977). Neutron dosimetry with solid state nuclear track detectors. Nuclear Track Detection, 1(3-4), 189-197.

[156] Liermann, J., Shinoto, M., Syed, M., Debus, J., Herfarth, K., & Naumann, P. (2020). Carbon ion radiotherapy in pancreatic cancer: a review of clinical data. Radiotherapy and Oncology, 147, 145-150.

[157] Ono, K. (2016). An analysis of the structure of the compound biological effectiveness factor. Journal of Radiation Research, 57(S1), i83-i89.

[158] Morris, G. M., Coderre, J. A., Hopewell, J. W., Micca, P. L., & Rezvani, M. (1994). Response of rat skin to boron neutron capture therapy with p-boronophenylalanine or borocaptate sodium. Radiotherapy and Oncology, 32(2), 144-153.

[159] Oed, A. (1995). Properties of micro-strip gas chambers (MSGC) and recent developments. Nuclear Instruments and Methods in Physics Research Section A: Accelerators, Spectrometers, Detectors and Associated Equipment, 367(1-3), 34-40.

[160] Buzulutskov, A. F. (2007). Radiation detectors based on gas electron multipliers. Instruments and experimental techniques, 50, 287-310.

[161] Giomataris, Y. (1998). Development and prospects of the new gaseous detector "Micromegas". Nuclear Instruments and Methods in Physics Research Section A: Accelerators, Spectrometers, Detectors and Associated Equipment, 419(2-3), 239-250.

[162] Fonte, P. (2002). Applications and new developments in resistive plate chambers. IEEE transactions on nuclear science, 49(3), 881-887.

[163] Gao, J., Xia, Z., Gunasekar, S., Jiang, C., Karp, J. M., & Joshi, N. (2024). Precision drug delivery to the central nervous system using engineered nanoparticles. Nature Reviews Materials, 9(8), 567-588.

[164] Elmaghraby, E. K., Abdelaal, S., Abdelhady, A. M., Fares, S., Salama, S., & Mansour, N. A. (2020). Experimental determination of the fission-neutron fluence-to-dose conversion factor. Nuclear Instruments and Methods in Physics Research Section A: Accelerators, Spectrometers, Detectors and Associated Equipment, 949, 162889.